Structural Monitoring and Maintenance, *Vol. 11, No. 4 (2024) 315-347*
https://doi.org/10.12989/smm.2024.11.4.315

Predicting of load capacity of concrete columns confined with FRP bars and subjected to axial compression at different eccentricity levels

Sarra Sendjasni[1a], Mohammed Berradia[*1], Riad Benzaid[2b] and Ali Raza[3c]

[1]*Department of Civil Engineering, Laboratory of Structures, Geotechnics and Risks (LSGR), Hassiba Benbouali University of Chlef, B.P 78C, Ouled Fares Chlef 02180, Algeria*
[2]*Department of Civil Engineering, L.G.G. Research laboratory, Jijel University, BP.96 Ouled Issa, Jijel-18000, Algeria*
[3]*Department of Civil Engineering, University of Engineering and Technology Taxila, 47080, Pakistan*

(*Received September 27, 2024, Revised November 28, 2024, Accepted November 29, 2024*)

Abstract. In this study, two new models were developed to predict the peak axial capacity of reinforced concrete (RC) compressive members having fiber-reinforced polymer (FRP) bars at different eccentricity levels (e/h = 0 and e/h ranges from 0.08 to 1) using two distinct methods: the general regression method and the eXtreme Gradient Boosting (XGBoost) algorithm. These models were developed based on a wide range dataset comprising tests data of 308 FRP-reinforced concrete samples compiled from the existing literature. Besides, the efficiency and accuracy of the proposed models were assessed using five statistical indicators namely, coefficient of determination (R^2), root mean square error (RMSE), mean absolute error (MAE), average absolute error (AAE), standard deviation (SD), and were equated with design codes and previously proposed formulas in the literature. The findings demonstrate that the suggested estimation models were suitable for capturing the axial capacity of FRP-RC compressive members. Particularly, the XGBoost model exhibited outstanding performance with a high R^2 value of 0.98 and minimal RMSE, MAE, AAE and SD values of 259.05 kN, 144.36 kN, 0.11, and 0.14 respectively, indicating excellent efficiency and accuracy compared to both the empirical model proposed and other existing models. This outcome highlights the ability of machine learning models to estimate the axial capacity of FRP-RC compressive members. Consequently, the XGBoost model offers a viable alternative method to empirical models for design applications.

Keywords: axial capacity; FRP bars; regression analysis; RC columns; XGBoost algorithm

1. Introduction

The primary function of a reinforced concrete compressive member is to support axial loads, regardless of whether they are accompanied by bending moments. However, the ability of steel bar reinforced concrete compressive members to carry axial loads diminishes over the design life of

*Corresponding author, Ph.D., E-mail: m.berradia@univ-chlef.dz
[a]Ph.D. Student, E-mail: s.sendjasni@univ-chlef.dz
[b]Professor, E-mail: r_benzaid@univ-jijel.dz
[c]Ph.D., E-mail: ali.raza@uettaxila.edu.pk

http://www.techno-press.org/?journal=smm&subpage=7 ISSN: 2288-6605 (Print), 2288-6613 (Online)

concrete structures due to corrosion of the steel bars. This problem is especially pronounced in coastal areas or harsh environmental conditions, presenting a major drawback of using steel-reinforced concrete in construction. As a result, the expenses associated with retrofitting and repairing deteriorated concrete structures are notably high (Alaa Hasan et *al*. 2019, Tarawneh *et al*. 2021, Karim et *al*. 2016, Chaallal and Benmokrane 1993, Abdalla *et al.* 2019, Alnemrawi and Al-Rousan 2024, Al-Rousan 2020a, Al-Rousan 2020b and Baili *et al*. 2022).

The review of the literature found that fiber-reinforced polymer (FRP) composites have been widely used as internal reinforcement (FRP reinforcing bars) in reinforced concrete structures due to their excellent corrosion resistance, high strength-weight ratio resistance to harsh environmental conditions (Sun 2024, Jabbar and Farid 2018, Ye *et al.* 2022). In this context, several studies have been carried out on the performance of FRP bars reinforced concrete columns under concentric compression (Pantelides *et al*. 2013, Tavassoli and Sheikh 2017, Raza *et al*. 2021, Al-Rousan 2022a, Al-Rousan 2022b, Al-Rousan and Alnemrawi 2023a, Al-Rousan and Alnemrawi 2023b, Al-Rousan and Barfed 2019, AlAjarmeh et *al*. 2022). The investigated parameters included the concrete compressive strength, gross cross-sectional area, cross-sectional area of FRP reinforcing bar, number of FRP bars, form of tie bar, type of longitudinal FRP reinforcement, type of transverse FRP reinforcement, diameter of stirrups, diameter of the main FRP bar, the elastic modulus of FRP bar and tensile strength of FRP bar, and spacing of stirrups. Experimental studies have shown that FRP bar-reinforced concrete compressive members exhibit lower load-carrying capacities under concentric axial loads than steel bar-reinforced concrete compressive members of identical size and reinforcement configuration. This disparity is mainly attributed to the reduced ultimate compressive strength and modulus of elasticity of FRP bars in compression, as compared to conventional steel bars (Alaa Hasan *et al*. 2019, Mohamed *et al*. 2014, Choo *et al*. 2006, Al-Rousan and Issa 2016, Al-Rousan and Sawalha 2024, Al-Rousan *et al.* 2024, Al-Rousan *et al*. 2022 and Issa *et al*. 2009). Additionally, neglecting the contribution of FRP bars will underestimate the axial capacity. According to Tobbi *et al*. (2014), the load–carrying capacity of concrete compressive members increases with considering the contribution of FRP bars. Similar to Tobbi *et al*. (2014), Elmessalami *et al*. (2019) concluded also that FRP bars can offer from 3%-14% of axial capacity. Theoretical models such as ACI 440.1R-15, CSA S806-02, CSA S806-12, AS-3600, Tobbi *et al*. (2012), Tobbi *et al*. (2014), Afifi *et al*. (2014a), Afifi *et al*. (2014b), Maranan et *al*. (2016), Xue *et al*. (2018), Mohammed *et al*. (2014a, b), Samani and Attard (2012), Khan *et al*. (2016), Hadhood *et al*. (2017) were established to predict the peak axial capacity of FRP bars reinforced concrete compressive members. The developed formulas were based on three main approaches: ignoring the contribution of FRP bars in compression, considering the contribution of FRP bars based on reduced tensile strength, and considering the contribution of FRP bars based on axial strain. Most of these models were suggested using regression analysis and based on limited test results. The difficulties of these models are that they cannot predict the peak axial capacity of FRP bars-reinforced concrete compressive members accurately. However, investigations on the performance of FRP bars reinforced concrete compressive members under eccentric compression are still limited and no suggested formulas existing in the literature considered the eccentricity effect.

In recent years, artificial intelligence (AI)-based machine-learning (ML) algorithms have been used popularly to solve structural engineering problems and more specifically, in the development of different prediction models of carrying capacities of FRP-RC compressive members (Bakouregui *et al*. 2021). Isleem *et al*. (2022) used (artificial neural network) ANN to predict the axial capacity of FRP-RC compressive members. Raza *et al*. (2022) used (artificial neural network) ANN to evaluate the structural response of GFRP-RC compressive members with normal strength concrete (NSC). Berradia *et al*. (2023) applied group method of data handling (GMDH) to

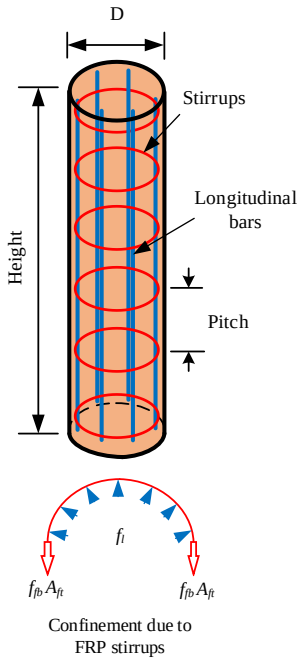

Fig. 1 Illustration of lateral confinement of FRP-RC columns

estimate the axial capacity of GFRP-RC compressive members. Nevertheless, there are very limited carrying capacity prediction models based on eXtreme Gradient Boosting (XGBoost) learning algorithms.

The present study proposes the application of the eXtreme Gradient Boosting (XGBoost) algorithm to predict the axial capacity of FRP-reinforced compressive members having different levels of eccentricity. This approach is unique, as it examines the development of an interpretable machine-learning model for capturing the axial capacity of FRP-reinforced compressive members with different levels of eccentricity (e⁄h ranges from 0 to 1), an area that has not been extensively investigated. Further, the proposed XGBoost model offers a potential alternative to available mechanics-based models for practical engineering design purposes. A comprehensive dataset containing experimental data of 308 FRP-reinforced concrete samples was collected from the previous studies. The efficiency and accuracy of the proposed models were compared with those fifteen empirical models. Five statistical indicators including coefficient of determination (R^2), Root mean square error (RMSE), Mean absolute error (MAE), Average absolute error (AAE), and standard deviation (SD) are calculated to assess the performance of those predictive models.

2. Review of design formulations of FRP-RC compressive members

So far, several investigations suggested design models for calculating the ultimate axial load-caring capacity (P_u) of FRP-RC compressive members. In this section, fifteen existing models will briefly summarize, including four models from current codes of ACI 440.1R-15, CSA S806-02, CSA S806-12 and AS-3600 and eleven empirical formulations developed by Tobbi *et al*. (2012),

Table 1 Existing design formulations of FRP-RC compressive members.

Reference	Section form	FRP type	Design formulas, P_u	
ACI 440.1R-15	-	FRP	$P_u = 0.85 f_c^{'}\left(A_g - A_{frp}\right)$	Eq. (1)
CSA S806-02	-	FRP	$P_u = 0.85 f_c^{'}\left(A_g - A_{frp}\right)$	Eq. (2)
CSA S806-12	-	FRP	$P_u = \alpha_1 f_c^{'}\left(A_g - A_{frp}\right)$ $\alpha_1 = 0.85 - 0.0015 f_c^{'} \geq 0.67$	Eq. (3)
AS-3600	-	FRP	$P_u = 0.85 f_c^{'}\left(A_g - A_{frp}\right) + 0.0025 E_{frp} A_{frp}$	Eq. (4)
Tobbi *et al.* (2012)	Square	GFRP	$P_u = \alpha_1 f_c^{'}\left(A_g - A_{frp}\right) + \alpha_{frp} f_{frp} A_{frp}$ $\alpha_1 = 0.85\,;\ \alpha_{frp} = 0.35$	Eq. (5)
Tobbi *et al*. (2014)	Square	GFRP	$P_u = 0.85 f_c^{'}\left(A_g - A_{frp}\right) + \varepsilon_{co} E_{frp} A_{frp}$ $\varepsilon_{co} = 0.003$	Eq. (6)
Afifi *et al*. (2014a)	Circular	CFRP	$P_u = \alpha_1 f_c^{'}\left(A_g - A_{frp}\right) + \alpha_{frp} f_{frp} A_{frp}$ $\alpha_1 = 0.85\,;\ \alpha_{frp} = 0.25$	Eq. (7)
Afifi *et al.* (2014b)	Circular	GFRP	$P_u = 0.85 f_c^{'}\left(A_g - A_{frp}\right) + \alpha_g f_{frp} A_{frp}$ $\alpha_g = 0.35$	Eq. (8)
Maranan *et al*. (2016)	Circular	GFRP	$P_u = \alpha_1 f_c^{'}\left(A_g - A_{frp}\right) + 0.002 E_{frp} A_{frp}$ $\alpha_1 = 0.9$	Eq. (9)
Xue *et al*. (2018)	Square	GFRP	$P_u = \alpha_1 f_c^{'}\left(A_g - A_{frp}\right) + 0.002 E_{frp} A_{frp}$ $\alpha_1 = 0.85$	Eq. (10)
Mohammed *et al*. (2014a)	Circular	GFRP CFRP	$P_u = 0.85 f_c^{'}\left(A_g - A_{frp}\right) + \varepsilon_p E_{frp} A_{frp}$ $\varepsilon_p = 0.002$	Eq. (11)
Mohammed *et al*. (2014b)	Circular	GFRP CFRP	$P_u = 0.9 f_c^{'}\left(A_g - A_{frp}\right) + \varepsilon_{fg} E_{frp} A_{frp}$ $\varepsilon_{fg} = 0.002$	Eq. (12)
Samani and Attard (2012)	-	-	$P_u = 0.85 f_c^{'}\left(A_g - A_{frp}\right) + 0.0025 E_{frp} A_{frp}$	Eq. (13)
Khan *et al.* (2016)	Circular	GFRP	$P_u = 0.85 f_c^{'}\left(A_g - A_{frp}\right) + \alpha E_{frp} A_{frp}$ $\alpha = 0.61$	Eq. (14)
Hadhood *et al*. (2017)	Circular	CFRP	$P_u = 0.85 f_c^{'}\left(A_g - A_{frp}\right) + \alpha E_{frp} A_{frp}$ $\alpha_1 = 0.85 - 0.0015 f_c^{'}$	Eq. (15)

Tobbi *et al*. (2014), Afifi *et al*. (2014a, b), Maranan *et al*. (2016), Xue *et al*. (2018), Mohammed et *al*. (2014a, b), Samani and Attard (2012), Khan *et al*. (2016) and Hadhood *et al*. (2017). The explanation details of all existing models with their expressions are reported in Table 1. The illustration of FRP-RC compressive members is shown in Fig. 1.

3. Collected test dataset

Numerous researchers conducted experimental investigations to study the axial behavior of concrete compressive members internally confined with FRP bars in the literature. In this section, a large dataset of 377 of FRP-RC compressive member samples as listed in Appendix A (Table I) was compiled from 42 experimental studies of De Luca *et al*. (2010), Tobbi *et al*. (2012), Afifi *et al*. (2014 a, b), Tobbi *et al*. (2014), Mohamed *et al*. (2014), Prachasaree et *al*. (2015), Maranan *et al*. (2016), Xiaochun *et al*. (2016), Hales *et al*. (2016), Hadi and Youssef (2016), Ali *et al.* (2016), Khan *et al.* (2016), Hadi *et al.* (2017), Elchalakani *et al.* (2017), Hadhood *et al.* (2017), Hadhood *et al.* (2017), Hadhood *et al.* (2017), Hadhood *et al.* (2017), Khorramian *et al.* (2017), Sun *et al.* (2017), Elchalakani *et al.* (2017), Hadhood *et al.* (2018), Hadhood *et al.* (2018), Zhang *et al.* (2018), Tabatabaei *et al.* (2018), Tu *et al.* (2019), Xue *et al.* (2018), Salah-Eldin *et al.* (2019), Salah-Eldin *et al.* (2019), Elchalakani *et al.* (2019), Othman *et al.* (2019), Dong *et al.* (2019), El-Gamal *et al.* (2020), Elchalakani *et al.* (2020), Abdelazim *et al.* (2020), Khorramian *et al.* (2020), Barua *et al.* (2020), El Messalami *et al.* (2021), Bakouregui *et al.* (2021), Afaq *et al.* (2023) published between the year 2010 and 2023. This dataset encompasses both circular and square cross-sections of FRP-RC compressive members, transversally reinforced with FRP hoops, spirals, and ties, as well as longitudinally reinforced with FRP bars under both concentric and eccentric axial loads. It includes 235 samples with circular cross-sections and 142 samples with square cross-sections. Among these, 219 samples were transversally confined with FRP spirals, 35 with FRP hoops, and 129 with FRP ties. The dataset covers three types of FRP reinforcements: carbon fiber-reinforced polymer (CFRP), glass fiber-reinforced polymer (GFRP), and basalt fiber-reinforced polymer (BFRP).

In this study, we systematically considered all parameters that influence the axial structural behavior of FRP-RC columns. The dataset provides comprehensive information on the geometric and material properties of unconfined concrete and FRP reinforcement, encompassing essential factors like cross-sectional dimensions, reinforcement types, and load eccentricity levels. These factors were incorporated to capture the interactions between concrete and FRP bars that affect axial load capacity. Each parameter was selected based on its documented impact in the literature and relevance to the structural response of FRP-RC compressive members. For instance, the elastic modulus and tensile strength of the FRP bars influence axial stiffness and load-bearing capacity, while geometric properties and cross-section type affect confinement and load distribution. By compiling a detailed dataset, we aimed to develop robust predictive models applicable across diverse design scenarios.

The parameters included in this dataset were chosen specifically for their effect on the axial capacity (P_u) of FRP-RC compressive members, accounting for both geometric and material properties of unconfined concrete and FRP reinforcement. For the geometric, the properties include the cross-section type of concrete (S_{type}), height of the sample (H), gross cross-sectional area (A_g). For the unconfined concrete properties presented include the compressive strength (f'_c). For the FRP, the important properties include, the cross-sectional area of the FRP reinforcing bar (A_{frp}), Percentage of FRP reinforcement (ρ_{frp}), number of FRP bars (n), form of tie bar (Form), type of longitudinal FRP reinforcement (l_{type}), type of transverse FRP reinforcement (t_{type}), the diameter of stirrups (d_s), the diameter of the main FRP bar (d_m), the elastic modulus of FRP bar (E_{frp}), the tensile strength of FRP bar (f_{frp}), and spacing of stirrups (S_v), α_1 and α_{frp} are the coefficients whilst the axial load condition (P_{cond}) (concentric or eccentric) was also given in Table 1.

A summary of the ranges of data and test results of the selected dataset is presented in

Appendix A (Table II). The values of height (H), gross cross-sectional area (A_g), the compressive strength of unconfined concrete (f'_c), Percentage of FRP reinforcement (ρ_{frp}), the cross-sectional area of FRP reinforcing bar (A_{frp}), number of FRP bars (n), the diameter of the main FRP bar (d_m), elastic modulus of FRP bar (E_{frp}), the tensile strength of FRP bar (f_{frp}), diameter of stirrups (d_s), spacing of stirrups (S_v), and axial capacity of FRP-RC compressive members (P_u) of the samples are in the range of 500 mm - 3730 mm, 12272 mm² - 372100 mm², 21 MPa - 90 MPa, 1 % - 5 %, 200 mm² - 3721 mm², 3 - 16, 8 mm - 25 mm, 39 GPa -151 GPa, 574 MPa - 2000 MPa, 4 mm - 13 mm, 30 mm - 305 mm, 90 kN - 15234 kN, respectively.

4. Performance of the existing models of FRP-RC compressive members

Four the statistical assessment of the existing suggested models for calculating the ultimate axial capacity (P_u) of FRP bars-RC compressive members based on the collected dataset reported in in Appendix A. Several performance indices were determined including, (R^2), (RMSE), (MAE), (AAE) and (SD). The mathematical explanations Eqs. (16)-(20) are given are follows

$$R^2 = \left(\frac{n\left(\sum_{i=1}^{n} x_i y_i\right) - \left(\sum_{i=1}^{n} x_i\right)\left(\sum_{i=1}^{n} y_i\right)}{\sqrt{\left[n\sum_{i=1}^{n} x_i^{\,2} - \left(\sum_{i=1}^{n} x_i\right)^2\right]\left[n\sum_{i=1}^{n} y_i^{\,2} - \left(\sum_{i=1}^{n} y_i\right)^2\right]}} \right)^2 \tag{16}$$

$$RMSE = \sqrt{\frac{1}{n}\sum_{i=1}^{n}\left(x_i - y_i\right)^2} \tag{17}$$

$$MAE = \frac{\sum_{i=o}^{n-1}\left|x_i - y_i\right|}{n} \tag{18}$$

$$AAE = \frac{1}{n}\sum_{i=1}^{n}\left|\frac{x_i - y_i}{y_i}\right| \tag{19}$$

$$SD = \sqrt{\frac{\sum_{i=1}^{n}\left|\frac{x_i}{y_i} - \left(\frac{x}{y}\right)_{average}\right|^2}{n-1}} \tag{20}$$

In which x_i, y_i refer to the experimental measurement values and the prediction values, respectively. n denotes the total number of datasets. Lower values of MAE and RMSE indicate a more accurate evaluation of the model. The value of R^2 ranges from 0 to 1; a value of R^2 higher than 0.8 and closer to 1 indicates a better fit of the model (Diboune *et al*. 2022). Lower values of AAE and SD indicate good coherence and better dispersion, respectively.

4.1 ACI 440.1R-15 model

Using the experimental dataset comprising 308 collected data points, the performance of the ACI 440.1R-15 model was evaluated. Fig. 2(a) presents the statistical indicator values, with R^2 = 0.70, RMSE = 909.12 kN, MAE = 662.12 kN, AAE = 0.80, and SD = 1.44. These statistical indicators indicate poor performance between the experimental and predicted values. This observation is clearly illustrated by the majority of data points lying above the 45° diagonal line, indicating high dispersion of the data points.

4.2 AS-3600 model

The assessment of the ALCC model from the AS-3600 code is depicted in Fig. 2(b). This figure illustrates that the majority of data points lie above the 45° diagonal line and the upper limit line of 40%, indicating that this model overestimates the ALCC values. Furthermore, the value of R^2 = 0.70 indicates a weak correlation between the predicted and experimental values. Additionally, the other indicators RMSE = 909.18 kN, MAE = 662.19 kN, AAE = 0.80, and SD = 1.44 confirm the poor performance of this model.

4.3 CSA S806-02 model

Fig. 2(c) illustrates the statistical evaluation of the ALCC model from the CSA S806-02 code, using the experimental dataset developed in the previous section. The evaluation of this figure suggests that the statistical indices of this model are comparable to those obtained for the ACI 440.1R-15 model and AS-3600 model. These indices confirm that the performance of this model remains consistent with that of the previously discussed models.

4.4 CSA S806-12 model

The ALCC model of CSA S806-12, designed for FRP-RC compressive members, underwent evaluation against 308 experimental data points. Fig. 2(d) displays a coefficient of correlation R^2 = 0.71, indicating a weak correlation between the experimental and predicted values. However, this model achieves minimum values for four other statistical indicators: RMSE = 846.58 kN, MAE = 651.92 kN, AAE = 0.74, and SD = 1.33. These indicators confirm the satisfactory performance of this model compared to the ACI 440.1R-15, AS-3600, and CSA S806-02 models.

4.5 Tobbi et al. (2012) model

The ALCC model developed by Tobbi *et al.* (2012) was assessed using 308 experimental data points and five statistical indices. As shown in Fig. 2(e), the indicators RMSE = 1245.82 kN, MAE = 861.72 kN, AAE = 1.10, and SD = 1.86 reach maximum values, indicating significant errors divergence and very high dispersion. Moreover, R^2 = 0.61 suggests a weak correlation between the experimental and predicted values, with all data points lying above the 45° diagonal line. Consequently, the performance of this model remains poor compared to the four previously evaluated models.

4.6 Samani and Attard. (2012) model

Fig. 2(f) compares the measured and experimentally determined axial capacity values for both the existing experimental studies and the Samani and Attard (2012) model sets. From this figure, it can be observed that the quality line (black line) is surrounded by the majority of the data points.

The Samani and Attard (2012) model has an R^2 value of 0.70, indicating a weak correlation between the predicted and experimental values. Other evaluation indices for the prediction results of the Samani and Attard (2012) model are presented in the same figure. The values of RMSE and MAE are 909.18 kN and 662.19 kN, respectively, indicating poor accuracy of the prediction values. However, the values of AAE and SD are 0.80 and 1.44, respectively, illustrating high dispersion in the estimated values. Consequently, the Samani and Attard (2012) offers a performance similar to the other previously evaluated models, except for the Tobbi *et al*. (2012) model.

4.7 Afifi et al. (2014a) model

The assessment of the predicted axial capacity values of the Afifi et *al.* (2014a) model, based on the verification data from the developed test dataset, is shown in Fig. 2(g). This figure illustrates that the correlation (R^2) between the calculated results and the test results is 0.63, with an RMSE of 1128.73 kN, MAE of 754.62 kN, AAE of 1.00, and SD of 1.74. The empirical prediction points can be evenly arranged in the upper part of the ideal line. These statistical indicators indicate that the Afifi *et al.* (2014a) model has a lower R^2 value, suggesting that it cannot adequately account for data variance, The RMSE and MAE values indicate poor prediction accuracy, while the AAE and SD values suggest satisfactory dispersion. In summary, the model proposed by Afifi et *al.* (2014a) exhibits poor performance compared to all other models previously studied.

4.8 Afifi et al. (2014b) model

Fig. 2h illustrates the evaluation results of the axial capacity model developed by Afifi *et al.* (2014b) against the 308 test results collected from the literature and reported in Appendix A. According to this figure, it can be observed that this model provides relatively similar statistical index values as the Afifi *et al.* (2014a) model. Consequently, the performance of the Afifi *et al.* (2014b) model is also poor compared to all other models.

4.9 Tobbi et al. (2014) model

To assess the performance of the proposed axial capacity model by Tobbi *et al*. (2014) and to verify the accuracy of this model in predicting test results, the statistical index values are shown in Fig. 2(i). In this figure, the more the predicted points by this model are located above the diagonal 45° line, and $R^2 = 0.70$, which demonstrates a poor correlation between the predicted and test results. On the other hand, there is a high percentage of data points in the low range of error (0-40%) with RMSE = 909.19 kN and MAE = 662.19 kN, confirming low accuracy. In the same figure, the values of AAE and SD are 0.80 and 1.44, respectively, demonstrating that prediction values have high dispersion. These observations indicate better performance of this model compared to the other models previously evaluated, except for the models of ACI440.1R-15, AS-

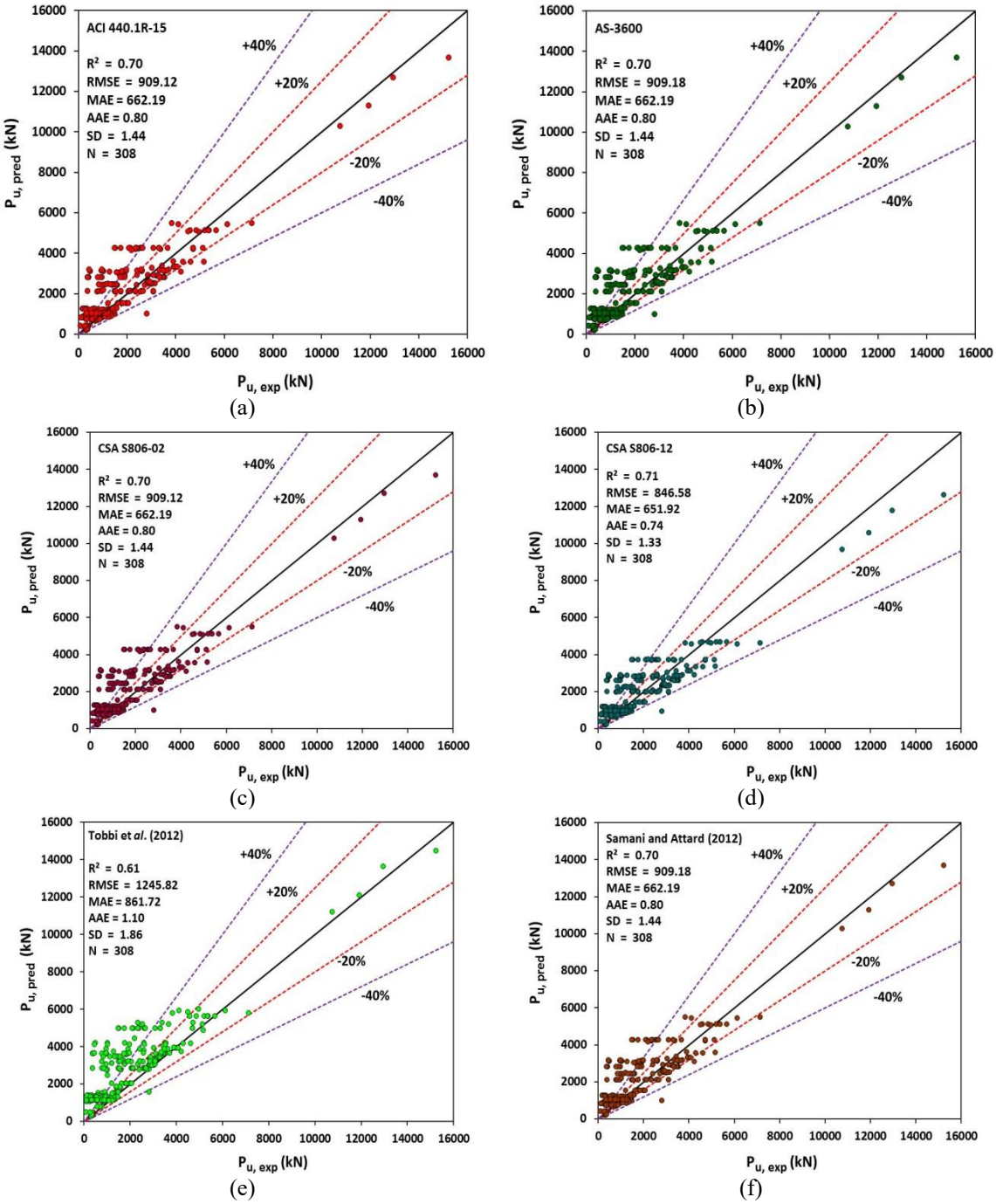

Fig. 2 Assessment results of existing calculation models of FRP-RC compressive members

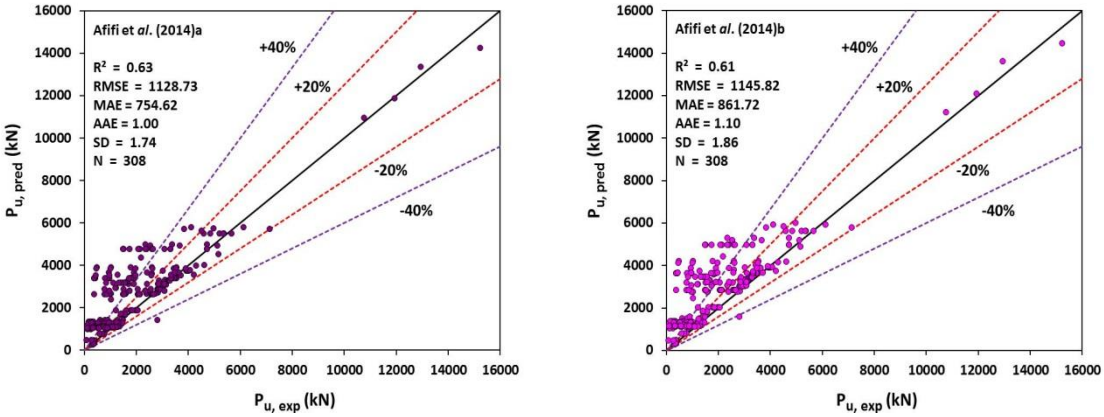

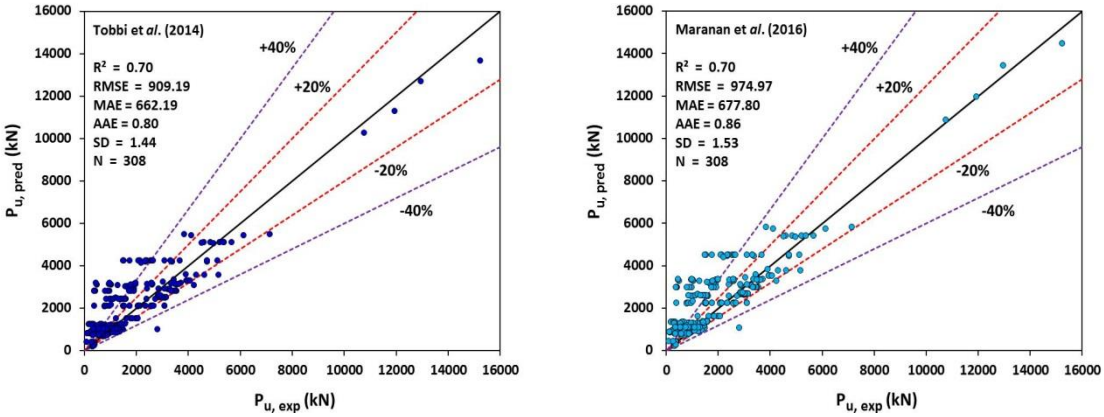

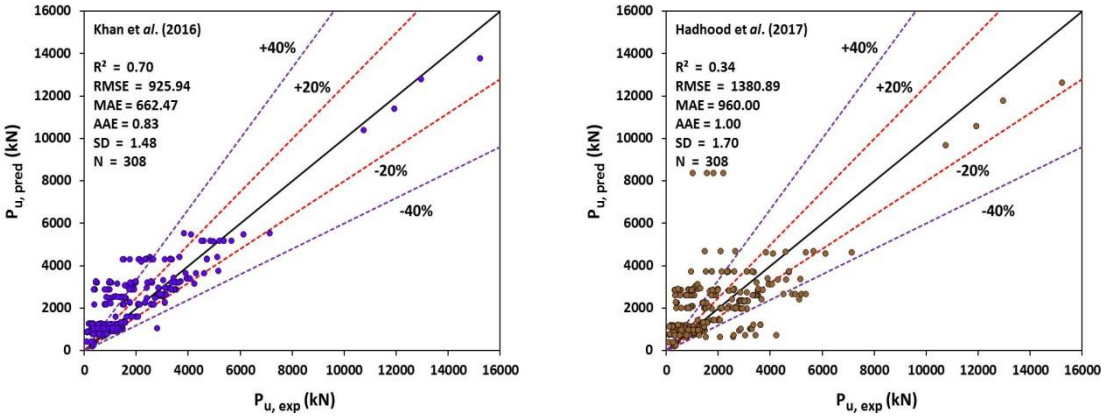

Fig. 2 Continued-

3600, CSA S806-02, CSA S806-12, and Samani and Attard (2012). These models show relatively similar predictions compared to the Tobbi *et al*. (2014) model.

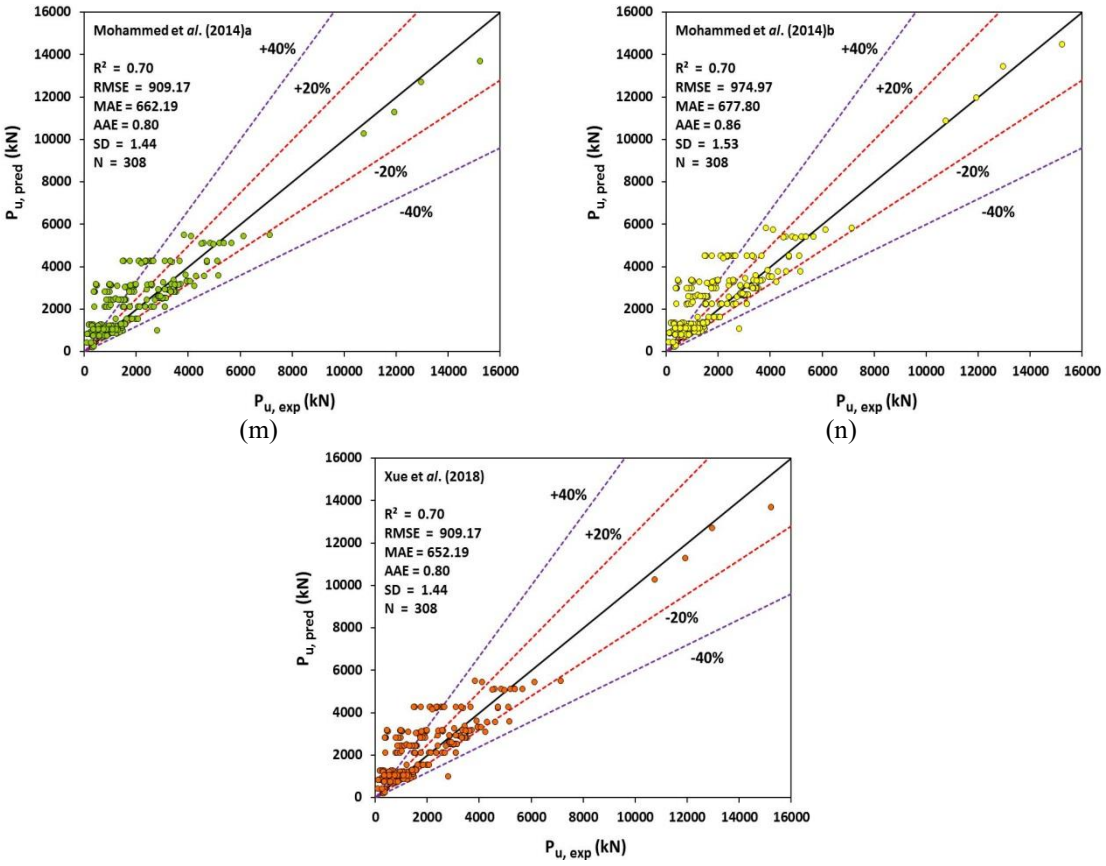

Fig. 2 Continued-

4.10 Maranan et al. (2016) model

The estimated and experimentally determined axial capacity values are compared in Fig. 2(j). In this figure, the statistical indicators R^2, RMSE, MAE, AAE, and SD are presented. The deviation values of the predicted values from the proposed model by Maranan *et al*. (2016) from the ideal line are also shown in the same figure. According to Diboune *et al*. (2022), if the linear correlation coefficient is greater than 0.8 and the RMSE, MAE, AAE, and SD are within a desirable range (considering the dispersion of the data points), it can be concluded that the experimental and predicted values are highly dependent. Regarding Fig. 2(j), it can be observed that the developed model has a correlation coefficient $R^2 = 0.70$. Additionally, based on the same figure, it can be seen that the error values obtained from the proposed model by Maranan *et al*. (2016) are RMSE = 974.97 kN, MAE = 677.80 kN, AAE = 0.86, and SD = 1.53. These statistical indicators demonstrate that this model has low accuracy and high dispersion of the estimation values. In summary, this model provides similar observations as the Tobbi *et al*. (2014) model.

4.11 Khan et al. (2016) model

Fig. 2(k) compares the predicted axial capacity values using the expression by Khan *et al*. (2016) with the developed 308 test results reported in Appendix A, where $P_{(u,pred)}$ represents the predicted values and $P_{(u,exp)}$ represents the experimental values. As evident from the model evaluation results, the R^2 of the model developed by Khan *et al*. (2016) is 0.70, which is far from 1 and smaller than 0.8. This indicates a poor correlation between the predicted and experimental values. The RMSE and MAE of Khan *et al*. (2016) model are 925.94 kN and 662.47 kN, respectively, with the majority of data points located in the error range of 0-40%. This suggests low accuracy. Additionally, the AAE and SD of this model are 0.83 and 1.48, respectively. These indicators show a high dispersion of the data points. Consequently, the observations from the assessment of this model are similar to the observations of the previous models studied in this section, except for the Tobbi *et al.* (2012) model, Afifi *et al*. (2014a, b) models.

4.12 Hadhood et al. (2017) model

The statistical evaluation of the Hadhood *et al*. (2017) model is conducted using the collected dataset. The results obtained are depicted in Fig. 2l. According to this figure, the value of R^2 = 0.34, indicates a poor correlation between the estimated and test values. This observation is clearly illustrated by the distribution of the majority of the data points below the diagonal 45° line. Additionally, the RMSE and MAE provide high values of 1380.89 kN and 960.00 kN, respectively, confirming the low accuracy of this model in predicting the experimental values. Moreover, this model exhibits a random scatter of points below the 45° diagonal and outside the upper limit line of 40%. This observation can be explained by the high values of AAE = 1.00 and SD = 1.70. The statistical indices indicate the weak performance of this model, which remains significantly lower compared to all other models.

4.13 Mohammed et al. (2014a) model

The Mohammed *et al*. (2014a) model is evaluated using the developed database. The outcomes are depicted in Fig. 2(m). According to this figure, the ALCC model's performance yields an R^2 value of 0.70, indicating a weak correlation between predicted and experimental values. This finding is evident from the dispersion of most points over the 45° diagonal. Similarly, the other statistical indices of RMSE = 909.17 kN and MAE = 662.19 kN present very high values; this indicates a poor and random distribution of the model, as indicated by AAE = 0.80 and SD = 1.44. Therefore, the performance of this model remains better than the Tobbi *et al*. (2012), Afifi *et al*. (2014a, b), Hadhood *et al*. (2017) models, and similar to the others previously mentioned.

4.14 Mohammed et al. (2014b) model

Fig. 2(n) presents the assessment of the axial capacity model developed by Mohammed *et al*. (2014b) using the 308 test results compiled from the literature. From this figure, it can be observed that this model provides relatively similar statistical index values as the Mohammed *et al.* (2014b) model (see Fig. 2(m)). Consequently, we can deduce that the performance of the Afifi *et al*. (2014b) model is also better than the Tobbi *et al*. (2012), Afifi *et al*. (2014a), Afifi *et al*. (2014b), Hadhood *et al.* (2017) models, and similar to the others previously mentioned.

4.15 Xue et al. (2018) model

In 2018, Xue *et al.* introduced a novel expression to compute the ALCC of FRP-RC compressive members. This section evaluates the performance of this model using 308 experimental data, as depicted in Fig. 2(o). The figure indicates an R^2 value of 0.70 alongside higher values of indicators such as RMSE = 909.17 kN, MAE = 652.19 kN, AAE = 0.80, and SD = 1.44. Additionally, the empirical prediction points may display an uneven distribution on both sides of the ideal line. These indices collectively signify the weak performance of this model, which aligns closely with the performance observed in all ALCC models assessed previously, except for the Tobbi *et al*. (2012), Afifi *et al*. (2014) a and b and Hadhood *et al*. (2017) models.

From this section, it can be concluded that all 15 existing models predict the ALCC of FRP-RC compressive members significantly higher compared to that of tests. In other words, the previous models predict the ALCC of FRP- RC compressive members more conservatively. Moreover, the results obtained from these models have a large Scattering with small values of R^2 ranging from 0.34 to 0.70 and low accuracy with high values of errors. This discrepancy is likely due to the effects of eccentricity was not considered in the published formulas.

5. Developing the predictive model using general regression analysis

This research primarily concentrates on formulating an empirical model to predict the ultimate axial capacity of FRP-RC compressive members under concentric and eccentric compression loads. Prior research has introduced several models for predicting the peak axial load-carrying capacity (ALCC) of FRP-RC compressive members. It's noteworthy that the concrete contribution to the empirically determined ALCC of FRP-RC compressive members remains consistent across all the proposed formulas. In essence, the variations in the empirically determined values of P_u for FRP-RC compressive members primarily stem from the differing concepts used in the various formulations to evaluate the contribution of FRP main bars. Among these models, fifteen formulations were taken from the literature and reported in Table 1. For example, ACI 440.1R-15 provided no recommendations for the contribution of longitudinal FRP bars. The CSA S806-12 allows for the longitudinal reinforcement of concrete compressive members with FRP bars. However, it recommends ignoring the influence of the FRP bars when capturing the peak ALCC of FRP-RC compressive members. Nevertheless, numerous research studies have found that neglecting the contribution of FRP main bars in compression could lead to a significant disparity between the empirically calculated ALCC and the experimentally obtained one for FRP-RC compressive members (Tobbi *et al*. 2012, Afifi *et al*. 2014, Hadi *et al*. 2016). Thus, several researchers suggested including the contribution of FRP main bars in the peak axial capacity of FRP-RC compressive members through different methods. One method is to obtain the stress in the FRP bars by assuming a linear stress-strain relationship (that is $\sigma_{frp} = E_{frp} \times \varepsilon_{frp}$). Maranan *et al*. (2016) Eq. (9), Xue *et al*. (2018) Eq. (10), and Mohammed *et al*. (2014) (a and b) Eqs. (11) and (12), Samani and Attard (2012) Eq. (13), and Hadhood *et al.* (2017) Eq. (15) have been estimated the axial load supported by FRP main bars based on the axial strain (ε_{frp}) in the FRP bars as well as their stiffness (E_{frp}), given by ε_{frp} E_{frp} A_{frp}. However, Maranan *et al*. (2016), Xue *et al*. (2018), Mohammed *et al*. (2014a, b) suggested taking ε_{frp} = 0.002, Samani and Attard (2012) recommended taking ε_{frp} = 0.0025, and Hadhood *et al*. (2017) suggested taking ε_{frp} = 0.0035. Whereas, other researchers such as Tobbi *et al*. (2012) Eq. (5), Afifi *et al*. (2014a), Afifi *et al*.

(2014b) Eqs. (7) and (8) have considered the contribution of FRP main bars by adding the axial load supported by FRP main bars, given by $\alpha_{frp}\ f_{frp}\ A_{frp}$, where f_{frp} is the tensile strength of the FRP bars, and α_{frp} is the reduction factor that shows the ratio between the strength of the FRP bar under compression and the tension strength of the FRP bars. Tobbi *et al*. (2012) and Afifi *et al*. (2014b) suggested taking $\alpha_{frp} = 0.35$, and Afifi *et al*. (2014a) recommended taking $\alpha_{frp} = 0.25$. It should be noted that several research studies have proposed different models for the ALCC, all based on a limited set of test data. Consequently, there is no consensus among previous research studies regarding a unified model to predict the ultimate ALCC of FRP-RC compressive members. This diversity can also be attributed to variations observed in the response of FRP bars when subjected to axial compression. On the other hand, no model exists in the literature to capture the axial capacity of FRP-RC compressive members under both concentric and eccentric compression loads. In this section, a new and simple model was developed to estimate the peak ALCC of FRP-RC compressive members based on regression analysis. Considering that the confinement effect of internal FRP bars on core concrete varies under different core concrete strengths, section forms, restraint levels, and concentric and eccentric compression loads (Ma *et al*. 2022). This method was employed to simulate the relationship between the input parameters (independent variables) and the output parameter (ALCC of FRP-RC compressive members), which is the dependent variable.

It should be noted that linear regression is one of the most commonly used equations in statistical procedures. In this context, the general form of linear regression that can be used to fit the independent and dependent variables is expressed as follows

$$Y = a_o + a_1X_1 + a_2X_2 + a_3X_3 + ... + a_nX_n \tag{21}$$

Or

$$Y = a_o + aX \tag{22}$$

Where Y is the output parameter (i,e., the dependent variable), X_1, X_2, X_3,… X_n are the input parameters (i,e., independent variables), a_o and a are the regression coefficients (Berradia *et al*. 2021, Berradia *et al*. 2022, Berradia *et al*. 2023).

Where $a = [a_1\ a_2\ a_3 \ldots a_n]$

Microsoft Office Excel (Version 10) was used to propose the new expression. To assess the optimal model, five performance indices, which include goodness of fit (R^2), root mean square error (RMSE), mean absolute error (MAE), Average absolute error (AAE), and standard deviation (SD), were used to measure the accuracy of the predictive model, as was done to evaluate the fifteen existing models. The expressions of these indicators are given by Eqs. (16)-(20).

The general form of the developed ALCC model was expressed by the following expression:

$$P_u = \alpha.f_c^{'}\left(A_g - A_{frp}\right) + \varepsilon_{reg}E_{frp}A_{frp} \tag{23}$$

Where α is the reduction factor indicating the ratio between the strength of the FRP bar under compression and the tension strength of the FRP bas, ε_{reg} represents the axial strain in the FRP bar, A_g is the area of cross-section, A_{frp} is the cross-sectional area of the FRP reinforcing bar.

A regression analysis has been conducted based on the available experimental data with eccentricity equal to 0, reported in Table 2 to obtain the reduction factor α and the optimal strain value ε_{reg} for the use in Eq. (23)

The regression analysis yielded α and β values of 0.85 and 0.0037, respectively. These values were used in Eq. (23) to calculate the carrying capacity of FRP-reinforced concrete compressive

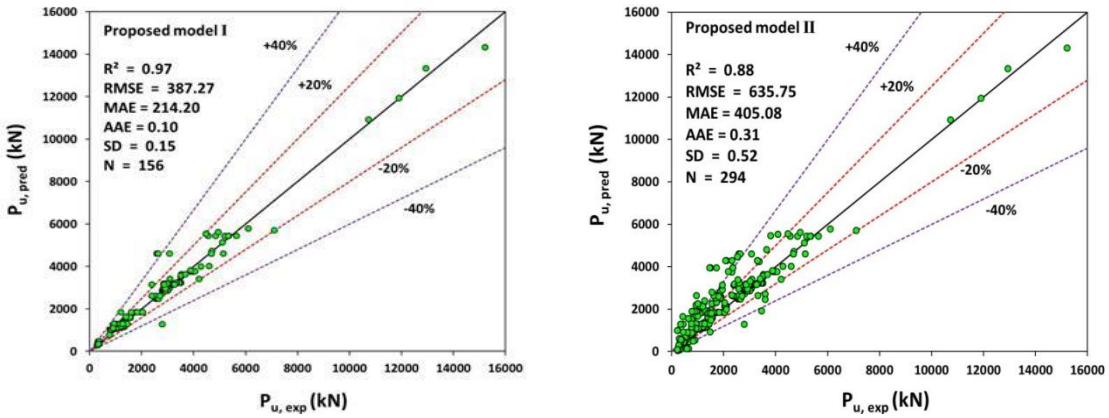

(a) Sample with (e/h = 0) (b) Sample with ((e)/h) ranges from 0 to 1

Fig. 3 Comparison between the predicted value and the experimental value of the carrying capacity of samples.

members under concentric compression loads. The final formula is expressed as follows

$$P_u = 0.85 f_c^{'}\left(A_g - A_{frp}\right) + 0.0037 E_{frp} A_{frp} \tag{24}$$

In this second part, the peak axial capacity was calculated for FRP-reinforced concrete compressive members at different eccentricity levels based on regression analysis. The calculation was applied on 294 FRP-RC compressive member samples reported in Appendix A (Table I) (14 FRP-RC compressive member samples were ignored). For this calculation, the Eq. (24) developed for the concentric compressive member was adopted.

According to Mahmoudabad *et al*. (2024) work, the increment in the eccentricity value reasonably decreased the axial capacity of the samples. For this reason, the proposed unified expression (model II) for calculating the peak axial capacity of FRP-RC compressive members at different eccentricity levels is formulated as follows

$$P_u = 0.85 f_c^{'}\left(A_g - A_{frp}\right) + 0.0037 E_{frp} A_{frp} - \gamma(e/h) \times \delta \times n \tag{25}$$

Where (e/h) is the eccentricity-sample dimension ratio and n is the number of FRP bars.

Through regression analysis of the experimental data with eccentricity-sample dimension ratio (e/h) ranges from 0 to 1, reported in Appendix A (Table I), the coefficient γ and δ values were obtained.

The final expression for calculating the peak axial capacity of FRP-reinforced concrete compressive members at different eccentricity levels is expressed as follows

$$P_u = 0.85 f_c^{'}\left(A_g - A_{frp}\right) + 0.0037 E_{frp} A_{frp} - 5.022(e/h) \times 100 \times n \tag{26}$$

Fig. 3 compares the predicted values of the peak axial capacity of FRP-RC samples with (e/h = 0) and FRP-RC samples with (e/h) ranges from 0 to 1 obtained by Eqs. (24) and (26), respectively, and the experimental values. From this figure, it can be seen that the equality line (black line) is surrounded by most of the data points. The model I has R^2 = 0.97, RMSE = 387.27 kN, MAE = 214.20 kN, AAE = 0.10, and SD = 0.15 and the model II has R^2 = 0.88, RMSE = 635.75 kN, MAE

= 405.08 kN, AAE = 0.31, and SD = 0.52. These indicator values show that the predicted value of the carrying capacity of the compressive members is in good agreement with the experimental value, which indicates that the models of carrying capacity proposed in this work have good predictability.

6. Developing the predictive model using eXtreme gradient boosting

6.1 Description of the eXtreme gradient boosting approach

XGBoost, short for eXtreme Gradient Boosting, is an ensemble machine-learning algorithm rooted in decision trees, essentially a composite predictor formed from numerous smaller predictors (Chen and Guestrin 2016). XGBoost consists of a collection of classification and regression trees, representing one of the most advanced and effective machine learning techniques developed in recent years. XGBoost constructs a sequential sequence of weak learners, with each learner trying to complement the others and correct any errors in the predictions made by preceding learners. XGBoost can manage missing data and utilizes regularization techniques to mitigate overfitting in individual predictors. It boasts a speedy implementation and achieves cutting-edge accuracy in both regression and classification tasks. Ultimately, XGBoost proves to be a potent approach for modeling nonlinear relationships (Bakouregui *et al*. 2021). The mathematical development model of XGBoost is shown as follows.

XGBoost represents an advanced enhancement of Friedman's original gradient-boosted trees model Friedman (2001). It employs an additive approach, wherein, for a dataset with n samples and m features denoted as $D = \{(X_i, Y_i)\}$, the prediction is expressed as follows

$$\hat{y}_i = \sum_{k=1}^{k} f_k(X_i),\ f_k \in F \tag{27}$$

Where F is the space of the regression tree, given by the following expression

$$F = \left\{ f(X) = w_q(x) \right\} \tag{28}$$

And k is the number of trees, Each f_k corresponds to an independent tree structure q and leaf weights w.

The aim formulation is

$$L = \sum_i l(\hat{y}_i, y_i) + \sum_k \Omega(f_k) \tag{29}$$

The prediction of the i-th instance at the t-th iteration is

$$\hat{y}_i^{(t)} = \hat{y}_{i-1}^{(t-1)} + f_l(X_i) \tag{30}$$

Therefore, the aim formulation can be expressed as follows

$$L^{(t)} = \sum_{i=1}^{n} l\left(y_i, \hat{y}_{i-1}^{(t-1)} + f_l(X_i)\right) + \Omega(f_k) \tag{31}$$

Where

$$\Omega(f_k) = \gamma T + \frac{1}{2}\lambda \sum_{j=1}^{T} w_j^2 \tag{32}$$

XGBoost utilyzes second-order Taylor approximation to optimize the aim formulation

$$L^{(t)} \approx \sum_{i=1}^{n}\left[l\left(y_i, \hat{y}_i^{(t-1)} + g_i f_t(X_i) + \frac{1}{2} h_i f_t^2(X_i) \right)\right] + \Omega(f_k) \tag{33}$$

Where

$$g_i = \frac{\partial l\left(y_i, \hat{y}_i^{(t-1)}\right)}{\partial \hat{y}_i^{(t-1)}} \tag{34}$$

And

$$h_i = \frac{\partial^2 l\left(y_i, \hat{y}_i^{(t-1)}\right)}{\partial \hat{y}_i^{(t-1)}} \tag{35}$$

The final aim formulation is given as follows

$$L^{(t)} = \sum_{i=1}^{n}\left[\left(g_i f_t(X_i) + \frac{1}{2} h_i f_t^2(X_i) \right)\right] + \gamma T + \frac{1}{2}\lambda \sum_{j=1}^{T} w_j^2 \tag{36}$$

$$L^{(t)} = \sum_{j=1}^{T}\left[\left(\sum_{i\in I_j} g_i \right) w_j + \frac{1}{2}\left(\sum_{i\in I_j} h_i + \lambda \right) w_j^2 \right] \tag{37}$$

The optimal weight w_j^* and the corresponding optimal value $\tilde{L}^{(t)}(q)$ leaf j are, respectively

$$w_j^* = -\frac{\sum_{i\in I_j} g_i}{\sum_{i\in I_j} h_i + \lambda} \tag{38}$$

$$\tilde{L}^{(t)}(q) = -\frac{1}{2}\sum_{j=1}^{T} \frac{\left(\sum_{i\in I_j} g_i \right)^2}{\sum_{i\in I_j} h_i + \lambda} + \gamma T \tag{39}$$

It's important to acknowledge that there are numerous programs available for data science and machine learning, with Python emerging as one of the most widely used programming languages. In this study, we employed the Python XGBoost library (Chen and Guestrin 2016) for tasks ranging from data preprocessing to model training and testing. Additionally, all data were initially arranged in Excel format (.xlsx) and subsequently imported and analyzed in Python utilizing the pandas package (Bakouregui *et al*. 2021).

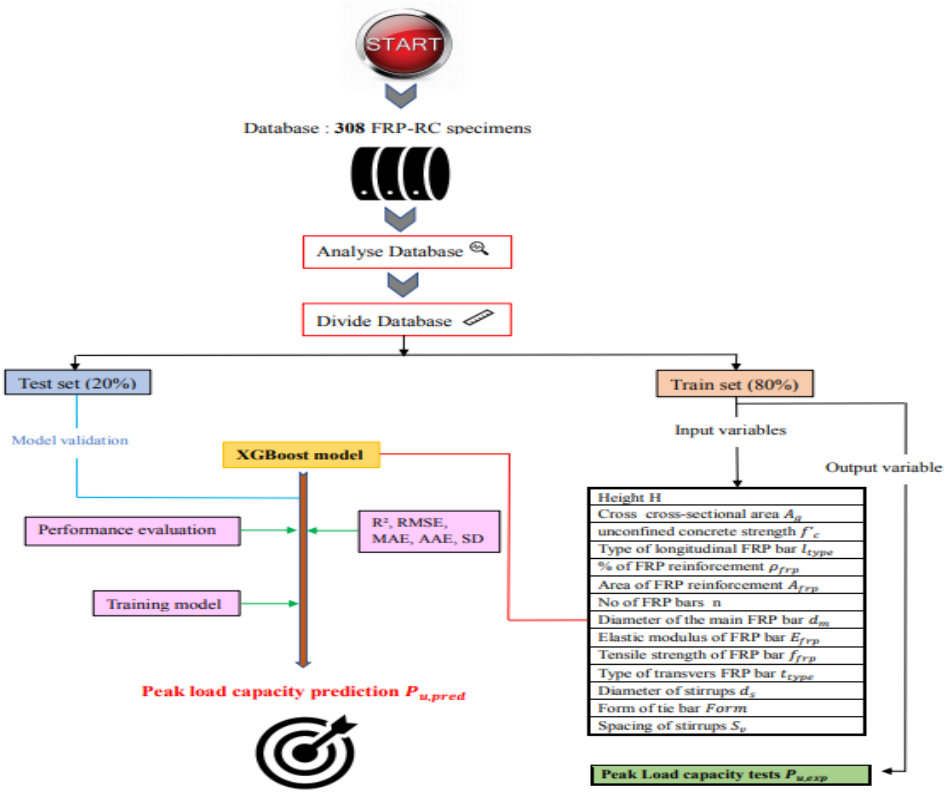

Fig. 4 Flow chart of XGBoost methodology

6.2 Detail of modeling

eXtreme Gradient Boosting (XGBoost) technique was utilized to obtain a meanihful relationship between the axial capacity of FRP-reinforced concrete compressive members and numerical and categorical variables listed in Appendix A (Table I). It should be noted that the XGBoost algorithm is suitable for processing numerical values. For this work, categorical independent parameters such as cross-section type of concrete (S_{type}), form of tie bar (Form), type of longitudinal FRP reinforcement (l_{type}) and type of transverse FRP reinforcement (t_{type}) were changed into new numerical independent parameters with the one hot encoding process before the start of the training and testing processes.

The XGBoost algorithm's basic model was chosen to be decision trees. The experimental dataset was divided into two groups at random to improve the model's capacity for generalization and reduce frequent problems such as overfitting. The testing group (20% or 61 FRP-RC samples) was set aside to evaluate the performance of the final XGBoost model on unobserved data, whereas the training group (80% or 247 FRP-RC samples) was used for modeling. The XGBoost approach is shown in Fig. 4.

A statistical evaluation was conducted to assess the performance and agreement of XGBoost model predictions using different statistical indicators such as coefficient of determination (R^2),

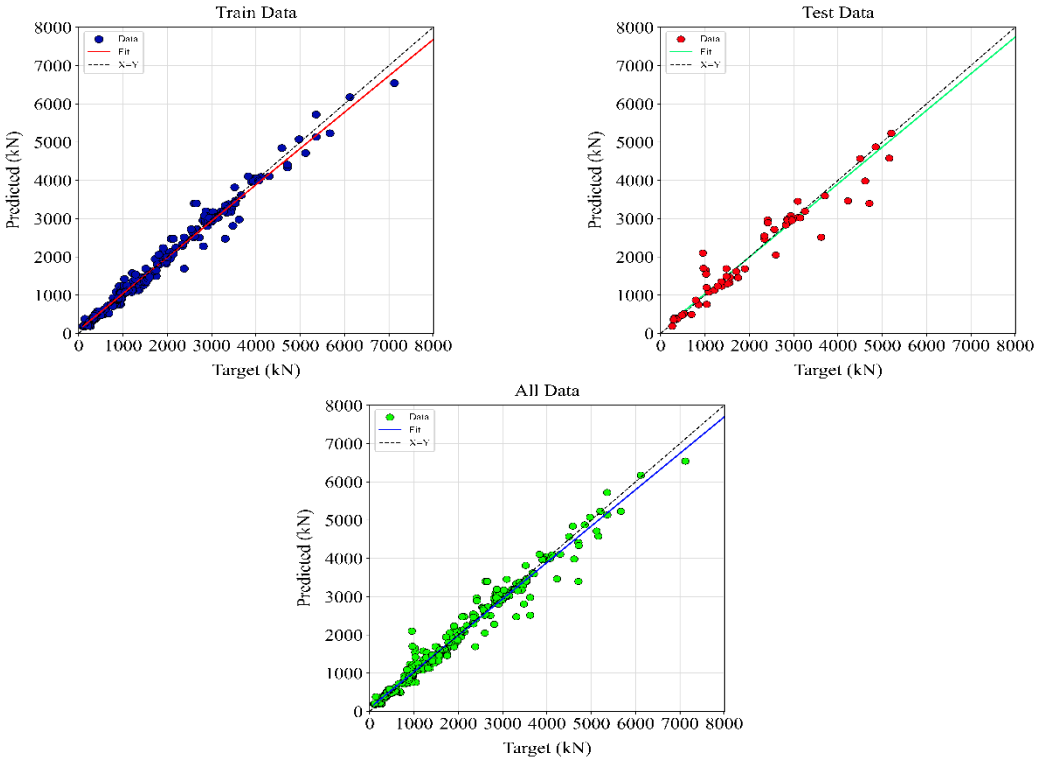

Fig. 5 Grid regression diagram after training

root mean square error (RMSE), mean absolute error (MAE), average absolute error (AAE), and standard deviation (SD) given by Eqs. (16)-(20). Then after, the best XGBoost model was derived by measuring statistically the goodness of fit and error values.

6.3 Discussion of research findings

The regression results for the XGBoost model are illustrated in Fig. 5 and Table 2. It can be seen from this figure that there is a strong correlation coefficient (R^2) (0.98 for training, 0.96 for testing, and 0.98 for whole) between the calculated and experimental values. In addition, the developed model is accurate enough to predict the axial capacity of FRP-reinforced concrete compressive members at different eccentricity levels. The developed XGBoost model presented the statistical indicators of RMSE = 222.52 kN, MAE = 123.97 kN, AAE = 0.10, SD = 0.13 for the training process, RMSE = 370.01 kN, MAE = 225.26 kN, AAE = 0.14, SD = 0.18 for the testing process, and RMSE = 259.05 kN, MAE = 144.36 kN, AAE = 0.11, SD = 0.14 for the whole datasets, as reported in Table 2.

Figs. 6(a)-6(c) compare the predicted values (P_{pred}) of the peak axial capacity of the FRP-RC compressive members obtained by the optimized XGBoost model and experimental values (P_{exp}). As it is presented in these figures, the relative difference between the predicted values (both from training, testing and whole sets) and the experimental values are very small, indicating a perfect agreement. Consequently, the prediction performance of the XGBoost model is excellent.

Table 2 A summary of performance indicators of the XGBoost algorithm

Statistical indicators	Training set	Testing set	All set
R^2	0.98	0.96	0.98
RMSE (kN)	222.52	370.01	259.05
MAE (kN)	123.97	225.26	144.36
AAE	0.10	0.14	0.11
SD	0.13	0.18	0.14

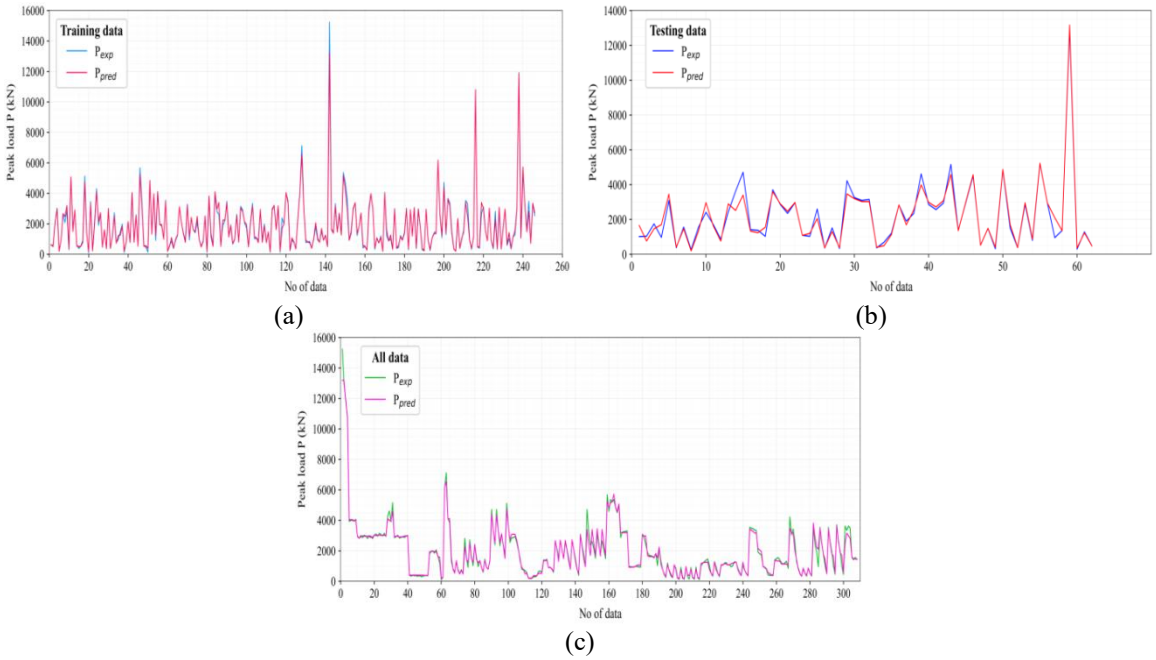

Fig. 6 Comparison between XGBoost predicted value P_{pred} and experimental value P_{exp}: (a) training data set, (b) testing data set, and (c) whole data set

From Fig. 7, the prediction capability of the developed model in terms of the normalized value ($P_{(u,pred)}/P_{(u,exp)}$) vs. the experimental axial capacity ($P_{(u,exp)}$) values can be illustrated. A ±20% error band is given in the graphic to show how the model's predictions and the experimental data differ from one another. As a reference point, the normalized value of 1.0 denotes an ideal estimation. The data primarily forms a tight cluster around this ideal line, indicating a close match between the experimental results and the predictions of the XGBoost model.

7. Comparison of XGBoost and empirical models with existing models

In Table 3 and Figs. 8(a)-8(e), the performance indicators R^2, RMSE, MAE, AAE, and SD of the models developed in this study and the previous research works (Table 1) in predicting the peak axial

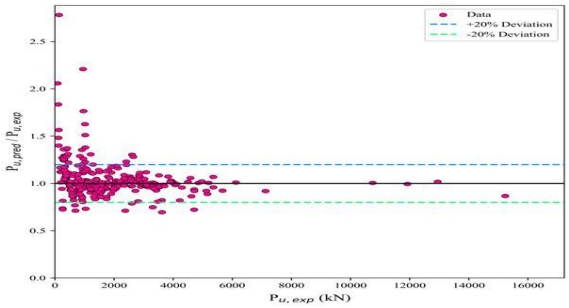

Fig. 7 Prediction capability of the XGBoost model in terms of the normalized value vs. the experimental axial capacity value

Table 3 Performance indicators of existing design formulations

Model	R^2	RMSE (kN)	MAE (kN)	AAE	SD
XGBoost model proposed	**0.98**	**259.05**	**144.36**	**0.11**	**0.14**
Empirical model proposed	**0.88**	**635.75**	**405.08**	**0.31**	**0.52**
ACI 440.1R-15	0.70	909.12	662.19	0.80	1.44
CSA S806-02	0.70	909.12	662.19	0.80	1.44
CSA S806-12	0.71	846.58	651.92	0.74	1.33
AS-3600	0.70	909.18	662.19	0.80	1.44
Tobbi *et al.* (2012)	0.61	1245.82	861.72	1.10	1.86
Tobbi *et al*. (2014)	0.70	909.19	662.19	0.80	1.44
Afifi *et al*. (2014a)	0.63	1128.73	754.62	1.00	1.74
Afifi *et al.* (2014b)	0.61	1145.82	861.72	1.10	1.86
Maranan et *al*. (2016)	0.70	974.97	677.80	0.86	1.53
Xue *et al*. (2018)	0.70	909.17	652.19	0.80	1.44
Mohammed *et al*. (2014a)	0.70	909.17	662.19	0.80	1.44
Mohammed *et al*. (2014b)	0.70	974.97	677.80	0.86	1.53
Samani and Attard (2012)	0.70	909.18	662.19	0.80	1.44
Khan *et al.* (2016)	0.70	925.94	662.47	0.83	1.48
Hadhood *et al*. (2017)	0.34	1380.89	960.00	1.00	1.70

capacity of FRP-reinforced concrete compressive members were compared. Table 3 and Fig. 8(a) visualizes that the proposed models have a better correlation between the predicted and experimental values (high R^2 values and very close to 1). On contrary, the other models give a low coefficient of determination R^2 values, ranging from 0.34 to 0.71. These findings show that the proposed models offer the best correlation compared to all of the other existing models. Table 3 and Figs. 8(b)-8(e) illustrate the comparison between the error values between the proposed models and the fifteen existing models. Form these figures, it can be noted the RMSE values of ACI 440.1R-15, CSA S806-02, CSA S806-12, AS-3600, Tobbi *et al*. (2012), Tobbi *et al*. (2014), Afifi *et al*. (2014a), Afifi *et al*. (2014b), Maranan *et al*. (2016), Xue *et al*. (2018), Mohammed *et al*. (2014a), Mohammed *et al*. (2014b),

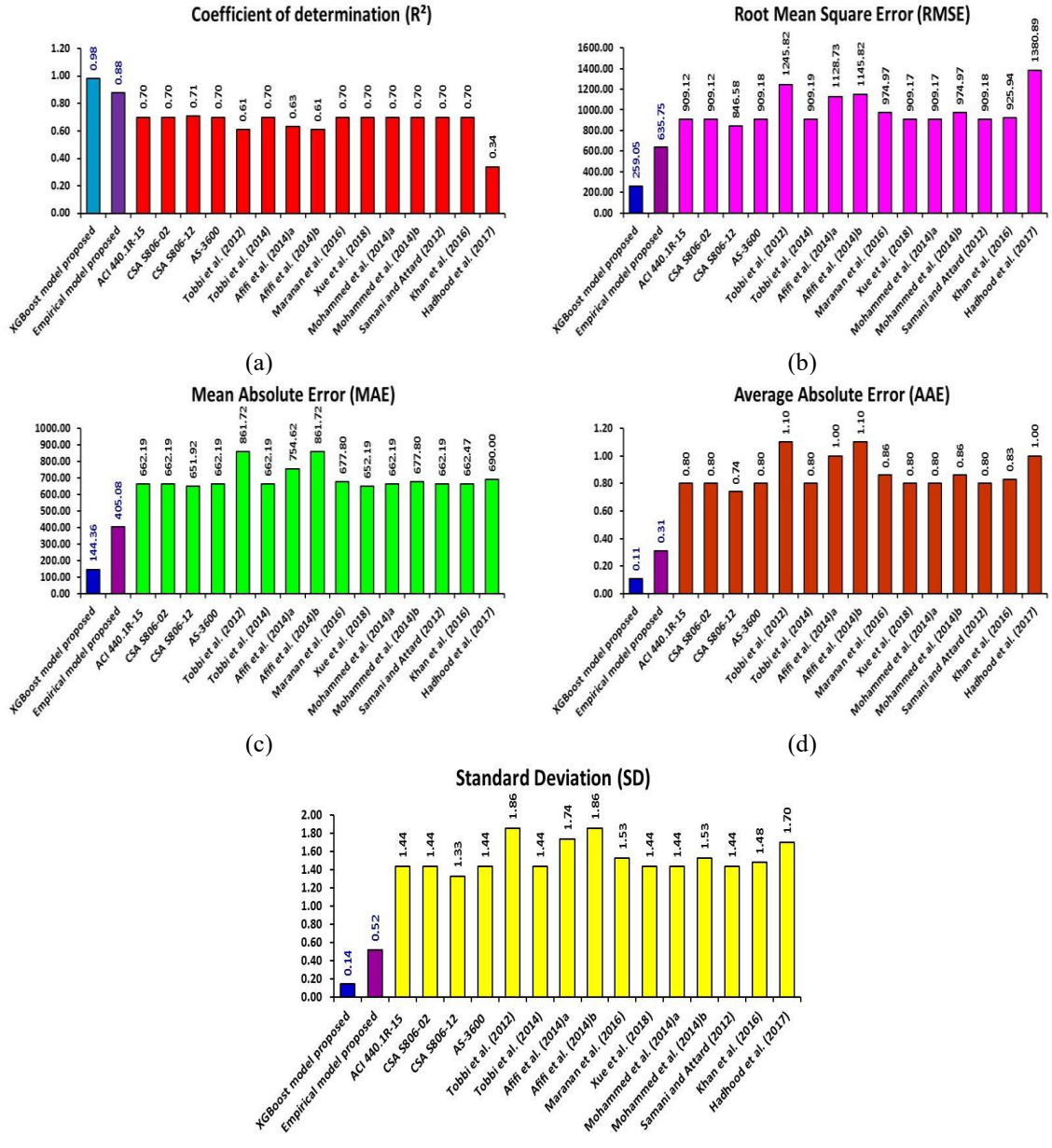

Fig. 8 Comparison of performance indicators of developed and existing models in predicting the ultimate axial capacity of FRP-reinforced concrete compressive members

Samani and Attard (2012), Khan *et al*. (2016), Hadhood *et al*. (2017) models are 909.12 kN, 909.12 kN, 846.58 kN, 909.18 kN, 909.19 kN, 1128.73 kN, 1145.82 kN, 974.97 kN, 909.17 kN, 909.17 kN, 974.97 kN, 909.18 kN, 925.94 kN, 1380.89 kN, respectively, whereas that of whole set of XGBoost and empirical models are only 259.05 kN and 635.75 kN, respectively. Similar to the RMSE results, the

proposed models have much lower MAE, AAE and SD values compared to the findings obtained from the other expressions. According to these indicators, it can be noted that the calculated results of the proposed models have a close agreement with the experimental results, which indicate the better accuracy of the proposed models in the prediction of the axial capacity of FRP bars reinforced concrete compressive members when compared to the existing expressions. Particularly, the XGBoost model exhibited outstanding performance with a high R^2value of 0.98 and minimal RMSE, MAE, AAE, and SD values of 259.05 kN, 144.36 kN, 0.11, and 0.14 respectively, indicating excellent efficiency and accuracy compared to both the empirical model proposed and other existing models. This outcome highlights the ability of machine learning models to estimate the axial capacity of FRP-RC compressive members. Consequently, the XGBoost model offers a viable alternative method to empirical models for design applications.

8. Conclusions

The present study aimed to assess the load-carrying capacity of reinforced concrete (RC) compressive members reinforced with FRP bars at varying eccentricity levels, using both empirical modeling and the eXtreme Gradient Boosting (XGBoost) algorithm. A comprehensive dataset comprising 308 test results on FRP-RC compressive members subjected to concentric and eccentric compression loads was analyzed. Utilizing this dataset, new empirical models and an XGBoost algorithm were developed to predict the load-carrying capacity of FRP-RC compressive members. These models are applicable to cases with eccentricity ratios (e/h) ranging from 0 to 1. Key conclusions drawn from this investigation are as follows:

1. A statistical evaluation of 15 existing models for predicting axial load-carrying capacity (ALCC) in FRP-reinforced concrete compressive members revealed that these models tend to overestimate capacity compared to test results, showing conservative estimates. Additionally, the predictions from these models displayed significant variability, with low R^2 values ranging from 0.34 to 0.70 and high error rates. This discrepancy is likely due to the lack of consideration for eccentricity effects in the existing formulas.
2. A regression analysis was conducted to derive new, simplified equations for calculating ALCC in FRP-RC compressive members. First, an expression specific to members under concentric compression was developed, incorporating the impact of FRP bars' axial strain (ε_{frp}) and stiffness (E_{frp}). Then, a unified expression for both concentric and eccentric compression loads (e/h from 0 to 1) was created, accounting for eccentricity effects.
3. The proposed empirical models demonstrated robust predictive performance over the test dataset. The first model, designed for concentric loading, achieved $R^2 = 0.97$, RMSE = 387.27 kN, MAE = 214.20 kN, AAE = 0.10, and SD = 0.15, indicating high precision and consistency. The second model, suitable for both concentric and eccentric loading, showed $R^2 = 0.88$, RMSE = 635.75 kN, MAE = 405.08 kN, AAE = 0.31, and SD = 0.52, highlighting its effective predictability across a wider range of load conditions.
4. The proposed XGBoost model exhibited exceptional predictive capability for the load-carrying capacity of FRP-RC compressive members, achieving an R^2 value of 0.98 and low error values (RMSE = 259.05 kN, MAE = 144.36 kN, AAE = 0.11, SD = 0.14). This indicates the model's superior precision and reliability in comparison to empirical models.
5. When compared to existing formulas, the XGBoost model consistently outperformed empirical models in accuracy. This suggests that both the empirical and XGBoost models

developed here offer reliable predictions for the load-carrying capacity of FRP-reinforced concrete compressive members under both concentric and eccentric loads, making them valuable tools for structural analysis and design applications.

Our study contributes to a more nuanced understanding of the behavior of FRP-reinforced concrete (FRP-RC) compressive members by demonstrating the effectiveness of machine learning techniques, specifically the XGBoost model, in predicting peak axial capacity. This predictive accuracy advances our understanding of FRP-RC behavior under varying eccentricity levels by providing reliable and data-driven estimates for complex structural scenarios that traditional empirical models may struggle to capture. The findings underscore the potential for machine learning to handle nonlinear relationships and variability in FRP-RC performance, offering insights that could lead to improved design codes and standards for FRP-reinforced members.

In terms of practical implications, the XGBoost model offers engineers a powerful tool for predicting axial capacity with high precision, which can be particularly useful in design scenarios where FRP materials are employed to enhance durability and corrosion resistance. This model could potentially streamline the design process by reducing the reliance on extensive physical testing and simplifying parameter selection for specific loading conditions. Moreover, by providing a viable alternative to empirical formulas, our approach has the potential to influence structural engineering practices in areas such as high-performance infrastructure and resilient construction, where FRP-RC systems are increasingly utilized.

Considering the limitation of the proposed models, the input parameters are acceptable within the range provided in Table 2. Future works are recommended on proposing explainable XGBoost tree-based prediction of axial capacity of FRP-reinforced self-compacting geopolymer concrete compressive members.

References

Alaa Hasan, H., Neaz Sheick, M. and Hadi, M.N.S. (2019), "Maximum axial load carrying capacity of fibre reinforced-polymer (FRP)", *Struct*, **19**, 227-233. https://doi.org/10.1016/j.istruc.2018.12.012.

Abdalla, K.M., Al-Rousan, R., Mohammad A. Alhassan, M.A. and Lagaros, N.D. (2019), "Finite Element Modelling of Concrete Filled Steel Tube Columns Wrapped With CFRP", *Proc. Inst. Civ. Eng.: Struct. and Build.*, **173**(11), 844-857. https://doi.org/10.1680/jstbu.19.00011.

Abdelazim, W., Mohamed, HM. and Benmokrane, B. (2020), "Inelastic second-order analysis for slender GFRP-reinforced concrete columns: Experimental investigations and theoretical study", *J. Compos. Constr.*, **24**(3), 04020016. https://doi.org/10.1061/(ASCE)CC.1943-5614.0001019.

ACI (2015), "American concrete institute, guide for the design and construction of concrete reinforced with FRP bars", In: ACI 4401R-15, ACI, Farmington Hills, MI.

Afaq, A., Bahrami, A., Alajarmeh, O., Chairman, N. and Yaqub, M. (2023), "Investigation of circular hollow concrete columns reinforced with GFRP bars and spirals", *Build*, **13**(4), 1056. https://doi.org/10.3390/buildings13041056.

Afifi, M.Z., Mohamed, H.M. and Benmokrane, B. (2014), "Axial capacity of circular concrete columns reinforced with GFRP bars and spirals", *J. Compos. Constr.*, **18**(1), 04013017. https://doi.org/10.1061/(ASCE)CC.1943-5614.0000438.

Afifi, M.Z., Mohamed, H.M. and Benmokrane, B. (2014), "Strength and axial behavior of circular concrete columns reinforced with CFRP bars and spirals", *J. Compos. Constr.*, **18**(2), 04013035. https://doi.org/10.1061/(ASCE)CC.1943-5614.0000430

AlAjarmeh, O., Manalo, A., Benmokrane, B., Schubel, P., Zeng, X., Ahmad, A., Hassanli, R. and Sorbello, C.D. (2022), "Compression behavior of GFRP bars under elevated In-Service temperatures", *Constr.*

Build. Mater., **314**, 125675. https://doi.org/10.1016/j.conbuildmat.2021.125675.
Ali, M.A. and El-Salakawy, E. (2016), "Seismic performance of GFRP-reinforced concrete rectangular columns", *J. Compos. Constr*., **20**(3), 04015074. https://doi.org/10.1061/(ASCE)CC.1943-5614.0000637.
Alnemrawi, B.R. and Al-Rousan, R. (2024), "The detailed axial compression behavior of CFST columns infilled by lightweight concrete", *Build*., **14**(9), 2844. https://doi.org/10.3390/buildings14092844
Al-Rousan, R. (2020a), "Behavior of circular reinforced concrete columns confined with CFRP composites", *Proc. Manuf*., **44**(1), 623-630. https://doi.org/10.1016/j.promfg.2020.02.247.
Al-Rousan, R.Z. (2020b), "Behavior of CFRP strengthened columns damaged by thermal shock", *Mag. Civ. Eng*., **97**(5), 9708. https://doi.org/10.18720/MCE.97.8.
Al-Rousan, R.Z. (2022a), "Cyclic behavior of alkali-silica reaction-damaged reinforced concrete beam-column joints strengthened with FRP composites", *Case. Stud. Constr. Mater*., **16**, e00869. https://doi.org/10.1016/j.cscm.2022.e00869.
Al-Rousan, R.Z. (2022b), "Cyclic lateral behavior of NLFEA heat-damaged circular CFT steel columns confined at the end with CFRP composites", *Case. Stud. Constr. Mater*., **17**, e01223. https://doi.org/10.1016/j.cscm.2022.e01223.
Al-Rousan, R.Z. and Alnemrawi, B.R. (2023a), "Behaviour of thermally shocked RC columns internally confined by auxetic steel wire mesh", *Proc. of the Inst. Civ. Eng. – Struct. Build*., **177**(10), 864-877. https://doi.org/10.1680/jstbu.22.00226.
Al-Rousan, R.Z. and Alnemrawi, B.R. (2023b), "Cyclic behavior of CFRP confined circular CFST damaged by alkali-silica reaction", *Int. J. Civ. Eng*., **21**, 1159-1180. https://doi.org/10.1007/s40999-023-00820-w.
Al-Rousan, R.Z. and Barfed, M.H. (2019), "Impact of curvature type on the behavior of slender reinforced concrete rectangular column confined with CFRP composite", *Compos. Part B*., **173**(1), 106939. https://doi.org/10.1016/j.compositesb.2019.106939.
Al-Rousan, R.Z. and Issa, M.A. (2016), "Stress-strain model and design guidelines for CFRP-confined circular reinforced concrete columns", *Polym. Compos*., **39**(8), https://doi.org/10.1002/pc.24262.
Al-Rousan, R.Z. and Sawalha, H.M. (2024), "The behavior of concrete filled steel tubular columns infilled with high-strength geopolymer recycled aggregate concrete", *Steel Compos. Struct*., **51**(6), 661-678. https://doi.org/10.12989/scs.2024.51.6.661.
Al-Rousan, R.Z., Bara'a R.A. and Sawalha, H.M. (2024), "The ultimate capacity of geopolymer recycled aggregate concrete filled steel tubular columns: Numerical and theoretical study", *J. Build. Eng*., **96**, 110365. https://doi.org/10.1016/j.jobe.2024.110365.
Al-Rousan, R.Z., Nusier, O., Abdalla, K., Alhassan, M. and Lagaros, N.D. (2022), "NLFEA of sulfate-damaged circular CFT steel columns confined with CFRP composites and subjected to axial and cyclic lateral loads", *Build*., **12**(3). https://doi.org/10.3390/buildings12030296.
AS 3600. (2018), "Concrete Structures", Standards Australia: Sydney, Australia.
Association CS. (2012), "Design and construction of building structures with fibre-reinforced polymer", CAN/CSA S806-12. Toronto, ON, Canada.
Baili, J., Raza, A., Azab, M., Ali, K., El Ouni, M., Haider, H. and Farooq, M.A. (2022), "Experiments and predictive modeling of optimized fiber-reinforced concrete columns having FRP rebars and hoops", *Mech. Adv. Mater. Struct*., **30**(23), 4913-4932. https://doi.org/10.1080/15376494.2022.2108527.
Bakouregui, A.S., Mohamed, H.M., Yahia, A. and Benmokrane, B. (2021), "Explainable extreme gradient boosting tree-based prediction of axial capacity of FRP-RC columns", *Eng. Struct.*, **245**, 112836. https://doi.org/10.1016/j.engstruct.2021.112836.
Barua, S. and El-Salakawy, E. (2020), "Performance of GFRP-reinforced concrete circular short columns under concentric, eccentric, and flexural loads", *J. Compos. Constr*., **24**(5), 04020044. https://doi.org/10.1061/(ASCE)CC.1943-5614.0001058.
Berradia, M., Azab, M., Ahmad, Z., Accouche, O., Raza, A. and Alashker, Y. (2022), "Data-driven prediction of compressive strength of FRP-confined concrete members: An application of machine learning models", *Struct. Eng. Mech.*, **83**(4), 515-535. https://doi.org/10.12989/sem.2022.83.4.515.
Berradia, M., El Ouni, M.H., Liaqat, A., Raza, A. and Ali, B. (2021), "Data-oriented analysis of axial capacity of externally CFRP-confined concrete columns transversely reinforced with steel hoops or

spirals", *Mech. Adv. Mater. Struct*., **28**(19), 1-14. https://doi.org/10.1080/15376494.2021.1980928
Berradia, M., Meziane, E.H, Raza, A., Ahmed, M., Zaman Khan, Q. and Shabbir, F. (2023), "Prediction of ultimate strain and strength of CFRP-wrapped normal and high-strength concrete compressive members using ANN approach", *Mech. Adv. Mater. Struct*., https://doi.org/10.1080/15376494.2023.22
Berradia, M., Meziane, E.H., Raza, A., El Ouni, M.H. and Shabbir, F. (2023), "A GMDH-based estimation model for axial load capacity of GFRP-RC circular columns", *Steel Compos. Struct*., **49**(2), 161-180. https://doi.org/10.12989/scs.2023.49.2.161.
CAN/CSA S806-02 (2006), "Design and construction of building structures with fibre-reinforced Polymers", Canadian standards association: Toronto, ON, Canada.
Chaallal, O. and Benmokrane, B. (1993), "Physical and mechanical performance of an innovative glass-fiber-reinforced plastic rod for concrete and grouted anchorages", *Can. J. Civ. Eng*., **20**(2), 254-268. https://doi.org/ 10.1139/l93-031.
Chen, T. and Guestrin, C. (2016), "XGBoost: A Scalable tree boosting system", *Proceedings of the 22nd ACM SIGKDD International Conference on Knowledge Discovery and Data Mining*, 785-94. https://doi.org/10.1145/2939672.2939785.
Choo, C.C., Harik, I.E. and Hans, G. (2006), "Strength of rectangular concrete columns reinforced with fiber-reinforced polymer bars", *ACI Struct J*., **103**(3), 452-459. https://doi.org/10.14359/15324.
De Luca, A., Matta, F. and Nanni, A. (2010), "Behavior of full-scale glass fiber-reinforced polymer reinforced concrete columns under axial load", *ACI Struct. J*., **107**(5), 589-596. https://doi.org/10.14359/51663912.
Diboune, N., Benzaid, R. and Berradia, M. (2022), "New strength–strain model and stress–strain relationship for square and rectangular concrete columns confined with CFRP wraps", *Mech. Adv. Mater. Struct.*, **30**(14), 2971-2994. https://doi.org/10.1080/15376494.2022.2067604.
Dong, M., Elchalakani, M., Karrech, A., Pham, T.M. and Yang, B. (2019), "Glass fibre-reinforced polymer circular alkali-activated fly ash/slag concrete members under combined loading", *Eng. Struct.*, **199**, 109598. https://doi.org/10.1016/j.engstruct.2019.109598.
Elchalakani, M. and Ma, G. (2017), "Tests of glass fibre reinforced polymer rectangular concrete columns subjected to concentric and eccentric axial loading", *Eng. Struct*., **151**, 93-104. https://doi.org/10.1016/j.engstruct.2017.08.023.
Elchalakani, M., Dong, M., Karrech, A., Li, G., Mohamed Ali, M. and Yang, B. (2019), "Experimental investigation of rectangular air-cured geopolymer concrete columns reinforced with GFRP bars and stirrups", *J. Compos. Constr*., **23**(3), 04019011. https://doi.org/10.1061/(ASCE)CC.1943-5614.0000938.
Elchalakani, M., Dong, M., Karrech, A., Mohamed Ali, M.S. and Huo, J.S. (2020), "Circular concrete columns and beams reinforced with GFRP bars and spirals under axial, eccentric, and flexural loading", *J. Compos. Constr*., **24**(3), 04020008. https://doi.org/10.1061/(ASCE)CC.1943-5614.0001008.
Elchalakani, M., Ma, G., Aslani, F. and Duan, W. (2017), "Design of GFRP-reinforced rectangular concrete columns under eccentric axial loading", *Mag. Concrete Res*., **69**(17), 865-77. https://doi.org/10.1680/jmacr.16.00437
El-Gamala, S. and AlShareedahb, O. (2020), "Behavior of axially loaded low strength concrete columns reinforced with GFRP bars and spirals", *Eng. Struct*., **216**, 110732. https://doi.org/10.1016/j.engstruct.2020.110732.
Elmesalami, N., El Refai, A. and Abed, F. (2019), "Fiber-reinforced polymers bars for compression reinforcement: A promising alternative to steel bars", *Constr. Build. Mater*., **209**(1), 725-737. https://doi.org/10.1016/j.conbuildmat.2019.03.105
ElMessalami, N., Abed, F. and El Refai, A. (2021), "Response of concrete columns reinforced with longitudinal and transverse BFRP bars under concentric and eccentric loading", *Compos. Struct.*, **255**, 113057. https://doi.org/10.1016/j.compstruct.2020.113057.
Hadhood, A., Mohamed, H.M. and Benmokrane, B. (2017), "Axial load–moment interaction diagram of circular concrete columns reinforced with CFRP bars and spirals: Experimental and theoretical investigations", *J. Compos. Constr*., **21**(2), 04016092. https://doi.org/10.1061/(ASCE)CC.1943-5614.0000748.

Hadhood, A., Mohamed, H.M. and Benmokrane, B. (2017), "Strength of circular HSC columns reinforced internally with carbon-fiberreinforced polymer bars under axial and eccentric loads", *Constr. Build. Mater.*, **141**(6), 366-378. https://doi.org/10.1016/j.conbuildmat.2017.02.117.

Hadhood, A., Mohamed, H.M. and Benmokrane, B. (2017), "Strength of circular HSC columns reinforced internally with carbon-fiber-reinforced polymer bars under axial and eccentric loads", *Constr. Build .Mater*., **141**, 366-378. https://doi.org/10.1016/j.conbuildmat.2017.02.117.

Hadhood, A., Mohamed, H.M. and Benmokrane, B. (2018), "Assessing stress-block parameters in designing circular high-strength concrete members reinforced with FRP bars", *J. Struct. Eng.*, **144**(10), 04018182. https://doi.org/10.1061/(ASCE)ST.1943-541X.0002173.

Hadhood, A., Mohamed, H.M. and Benmokrane, B. (2018), "Flexural stiffness of GFRP-and CFRP-RC circular members under eccentric loads based on experimental and curvature analysis", *ACI Struct. J.,* **115**(4), 1185-98. https://doi.org/10.14359/51702235.

Hadhood, A., Mohamed, H.M., Ghrib, F. and Benmokrane, B. (2017), "Efficiency of glass-fiber reinforced-polymer (GFRP) discrete hoops and bars in concrete columns under combined axial and flexural loads", *Compos. Part B: Eng*., **114**, 223-236. https://doi.org/10.1016/j.compositesb.2017.01.063.

Hadi, M.N. and Youssef, J. (2016), "Experimental investigation of GFRP-reinforced and GFRP-encased square concrete samples under axial and eccentric load, and four-point bending test", *J. Compos. Constr*., **20**(5), 04016020. https://doi.org/10.1061/(ASCE)CC.1943-5614.0000675.

Hadi, M.N., Hasan, H.A. and Sheikh, M.N. (2017), "Experimental investigation of circular high-strength concrete columns reinforced with glass fiber-reinforced polymer bars and helices under different loading conditions", *J. Compos. Constr*., **21**(4), 04017005. https://doi.org/10.1061/(ASCE)CC.1943-5614.0000784.

Hadi, M.N., Karim, H. and Sheikh, M.N. (2016), "Experimental investigations on circular concrete columns reinforced with GFRP bars and helices under different loading conditions", *J. Compos. Const*r, **20**(4), 04016009. https://doi.org/10.1061/(ASCE)CC.1943-5614.0000670.

Hales, T.A., Pantelides, C.P. and Reaveley, L.D. (2016), "Experimental evaluation of slender high-strength concrete columns with GFRP and hybrid reinforcement", *J. Compos. Constr*., **20**(6), 04016050. https://doi.org/10.1061/(ASCE)CC.1943-5614.0000709.

Isleem, H.F., Tayeh, B.A., Abid, M., Iqbal, M., Mohamed, A.M. and El Sherbiny, M.G. (2022), "Finite element and artificial neural network modeling of FRP-RC columns under axial compression loading", *Struct. Mater*., **9**. https://doi.org/10.3389/fmats.2022.888909.

Issa, M.A., Al-Rousan, R.Z. and Issa, M.A. (2009), "Experimental and Parametric Study of Columns with CFRP Composites", *J. Compos. Constr*., **13**(2), 135-147. https://doi.org/10.1061/(ASCE)1090-0268(2009)13:2(135).

Jabbar, S.A. and Farid, S.B. (2018), "Replacement of steel rebars by GFRP rebars in the concrete structures", *Karb Int. J. Moder Sci*., **4**(2), 216-227. https://doi.org/ 10.1016/j.kijoms.2018.02.002.

Karim, H., Sheikh, M.N. and Hadi, M.N.S. (2016), "Axial load-axial deformation behaviour of circular concrete columns reinforced with GFRP bars and helices", *Constr. Build Mater*., **112**(6-7), 1147-1157. https://doi.org/10.1016/j.conbuildmat.2016.02.219.

Khan, Q.S., Sheikh, M.N. and Hadi, M.N. (2016), "Axial-flexural interactions of GFRP-CFFT columns with and without reinforcing GFRP bars", *J. Compos. Constr*., **21**(3), 04016109. https://doi.org/10.1061/(ASCE)CC.1943-5614.0000771

Khorramian, K. and Sadeghian, P. (2017), "Experimental and analytical behavior of short concrete columns reinforced with GFRP bars under eccentric loading", *Eng. Struct.*, **151**, 761-773. https://doi.org/10.1016/j.engstruct.2017.08.064.

Khorramian, K. and Sadeghian, P. (2020), "Experimental investigation of short and slender rectangular concrete columns reinforced with GFRP bars under eccentric axial loads", *J. Compos. Constr*., **24**(6), 04020072. https://doi.org/10.1061/(ASCE)CC.1943-5614.0001088.

Ma, L., Zhou, C., Lee, D. and Zhang, J. (2022), "Prediction of axial compressive capacity of CFRP-confined concrete-filled steel tubular short columns based on XGBoost algorithm", *Eng. Struct*., **260**, 114239. https://doi.org/10.1016/j.engstruct.2022.114239.

Mahmoudabad, N.S., Bahrami, A., Saghir, S., Ahmed, A., Iqbal, M., Elchalakini, M. and Özkılıç, Y.O. (2024), "Effects of eccentric loading on performance of concrete columns reinforced with glass fiber-reinforced polymer bars", *Sci. Rep*., **14**(1), 1890. https://doi.org/ 10.1038/s41598-023-47609-4.

Maranan, G., Manalo, A., Benmokrane, B., Karunasena, W. and Mendis, P. (2018), "Behavior of concentrically loaded geopolymer-concrete circular columns reinforced longitudinally and transversely with GFRP bars", *Eng. Struct*., **117**, 422-436. https://doi.org/10.1016/j.engstruct.2016.03.036.

Mohamed, H., Afifi, M. and Benmokrane, B. (2014), "Performance evaluation of concrete columns reinforced longitudinally with FRP bars and confined with FRP hoops and spirals under axial load", *J. Brid Eng*., **19**(7), 04014020. https://doi.org/10.1061/(ASCE)BE.1943-5592.0000590.

Othman, ZS. and Mohammad, AH. (2019), "Behaviour of eccentric concrete columns reinforced with carbon fibre-reinforced polymer bars", *Adv. Civ. Eng*., **2019**, 1-13. https://doi.org/10.1155/2019/1769212.

Pantelides, C.P., Gibbons, M.E. and Reaveley, L.D. (2013), "Axial load behavior of concrete columns confined with GFRP spirals", *J. Compos. Constr*., **17**(3). https://doi.org/305-313. 10.1061/(ASCE)CC.1943-5614.0000357.

Prachasaree, W., Piriyakootorn, S., Sangsrijun, A. and Limkatanyu, S. (2015), "Behavior and performance of GFRP reinforced concrete columns with various types of stirrups", *Int. J. Polym. Sci*., **2015**(3), 1-9. https://doi.org/10.1155/2015/237231.

Raza, A., El Ouni, M.H. and Baili, J. (2022), "Data-driven analysis on axial strength of GFRP-NSC columns based on practical artificial neural network tool", *Compos. Struct*., **291**, 115598. https://doi.org/10.1016/j.compstruct.2022.115598.

Raza, A. and Ahmad, A. (2021), "Investigation of HFRC columns reinforced with GFRP bars and spirals under concentric and eccentric loadings", *Eng. Struct*., **227**. https://doi.org/111461. 10.1016/j.engstruct.2020.111461.

Salah-Eldin, A., Mohamed, H.M. and Benmokrane, B. (2019), "Axial–flexural performance of high-strength-concrete bridge compression members reinforced with basalt-FRP bars and ties: Experimental and theoretical investigation", *J. Brid Eng*., **24**(7), 04019069. https://doi.org/10.1061/(ASCE)BE.1943-5592.0001448.

Salah-Eldin, A., Mohamed, H.M. and Benmokrane, B. (2019), "Structural performance of high-strength-concrete columns reinforced with GFRP bars and ties subjected to eccentric loads", *Eng. Struct*., **185**, 286-300. https://doi.org/10.1016/j.engstruct.2019.01.143.

Samani, A.K. and Attard, M.M. (2012), "A stress–strain model for uniaxial and confined concrete under compression", *Eng. Struct*., **41**, 335-349. https://doi.org/10.1016/j.engstruct.2012.03.027.

Sun, L., Wei, M. and Zhang. N. (2017), "Experimental study on the behavior of GFRP reinforced concrete columns under eccentric axial load", *Constr. Build. Mater*., **152**, 214-225. https://doi.org/10.1016/j.conbuildmat.2017.06.159.

Sun, Y. (2024), "Estimation of compressive strength for spiral stirrup-confined circular concrete column using optimized machine learning with interpretable techniques", *Mech. Adv. Mater. Struct*., https://doi.org/10.1080/15376494.2023.2298232.

Tabatabaei, A., Eslami, A., Mohamed, H.M. and Benmokrane, B. (2018), "Strength of compression lap-spliced GFRP bars in concrete columns with different splice lengths", *Constr. Build. Mater*., **182**, 657-669. https://doi.org/10.1016/j.conbuildmat.2018.06.154.

Tarawneh, A.N., Dwairi, H.M., Almasabha, G.S. and Majdalawey, S.A. (2021), "Effect of fiber reinforced polymer-compression reinforcement in columns subjected to concentric and eccentric loading", *ACI Struct. J*., **118** (3), 187-197.

Tavassoli, A. and Sheikh, S.A. (2017), "Seismic resistance of circular columns reinforced with steel and GFRP", J. Compos for Constr, **21**(4), 04017002. https://doi.org/10.1061/(ASCE)CC.1943-5614.0000774.

Tobbi, H., Farghaly, A.S. and Benmokrane, B. (2012), "Concrete columns reinforced longitudinally and transversally with glass fiber-reinforced polymer bars", *ACI Struct. J*., **109**(4), 551-558. https://doi.org/10.14359/51683874.

Tobbi, H., Farghaly, AS. and Benmokrane, B. (2014), "Behavior of concentrically loaded fiber-reinforced polymer reinforced concrete columns with varying reinforcement types and ratios", *ACI Struct. J*., **111**(2),

375-386. https://doi.org/10.14359/51686528.
Tu, J., Gao, K., He, L. and Li, X. (2019), "Experimental study on the axial compression performance of GFRP-reinforced concrete square columns", *Adv. Struct. Eng*., **22**(7), 1554-1565. https://doi.org/10.1177/1369433218817988.
Xiaochun, F. and Zhang, M. (2016), "Behaviour of inorganic polymer concrete columns reinforced with basalt FRP bars under eccentric compression: An experimental study", *Compos. Part B*, **104**, 44-56. http://dx.doi.org/10.1016/j.compositesb.2016.08.020.
Xue, W., Peng, F. and Fang, Z. (2018), "Behavior and Design of Slender Rectangular Concrete Columns Longitudinally Reinforced with Fiber-Reinforced Polymer Bars", *ACI Struct. J*., **115**(2). https://doi.org/10.14359/51701131.
Xue, W., Peng, F. and Fang, Z. (2018), "Behavior and design of slender rectangular concrete columns longitudinally reinforced with fiber-reinforced polymer bars", *ACI Struct. J*., **115**(2), 311-322. https://doi.org/10.14359/51701131.
Ye, Y.Y., Zhuge, Y., Smith, S.T., Zeng, J.J. and Bai, Y.L. (2022), "Behavior of GFRP-RC columns under axial compression: Assessment of existing models and a new axial load-strain model", *J. Build. Eng*., **47**, 103782. https://doi.org/10.1016/j.jobe.2021.103782.
Zhang, X. and Deng, Z. (2018), "Experimental study and theoretical analysis on axial compressive behavior of concrete columns reinforced with GFRP bars and PVA fibers", *Constr. Build. Mater*., **172**, 519-532. https://doi.org/10.1016/j.conbuildmat.2018.03.237.

JK

Abbreviations

Acronyms

AAE	Average Absolute Error
ACI	American Concrete Institute
AI	Artificial intelligence
ALCC	Axial load carrying capacity
ANN	Artificial neural network
BFRP	Basalt fiber-reinforced polymer
CFRP	Carbon fiber-reinforced polymer
GFRP	Glass fiber-reinforced polymer
RC	Reinforced Concrete
FRP	Fiber Reinforced Polymer
R^2	Coefficient of determination
RMSE	Root mean square error
MAE	Mean Absolute Error
ML	Machine learning
NSC	Normal Strength Concrete
SD	Standard Deviation
GFRP	Glass fiber-reinforced polymer
GMDH	Group Method of Data Handling
XGBoost	EXtreme Gradient Boosting

Symbols

H	Height of the specimen
A_{frp}	Cross-sectional area of FRP reinforcing bar
A_g	Gross cross-sectional area
a , a_o	Regression coefficient
l_{type}	Type of FRP reinforcement
S_{type}	cross-section type of concrete
CS	Configuration of stirrups
C_{type}	Type of concrete
d_m	Diameter of main FRP bar
d_s	Diameter of stirrups
e	eccentricity
E_{frp}	Elastic modulus of FRP
$f_c^{'}$	Compressive strength of concrete
f_{frp}	Tensile strength of FRP
n	No. of FRP bars
N	Total number of datasets
$N_{normalized}$	Normalized value
ρ_{frp}	Percentage of FRP reinforcement
P_u	Ultimate axial capacity
P_{cond}	Axial Load Condition

$P_{u,pred}$	Predicted values of ultimate axial capacity
$P_{u,\exp}$	Experimental values of ultimate axial capacity
X_i	Experimental value
Y_i	Prediction value
X	Input parameters
Y	Output parameter
S_v	Spacing of stirrups
T_{type}	Type of tie bar
U_i	Predicted value
ε_{reg}	Axial strain in The FRP Bar
α_{frp}	Strength of the FRP bars
$\hat{y}_i$	Predicted output for the i-th instance.
$L^{(t)}$	The total loss function at the t-th iteration
$f_l(X_i)$	The output of the t-th base model for input Xi.
$\Omega(f_k)$	Regularization term that penalizes the complexity of the base mode
γ	Parameter that controls the penalty for adding additional leaves to the tree
T	The number of leaves in the tree
λ	Regularization parameter that controls the penalty on the leaf weights.
w_j	Weight of the j-th leaf.

Appendix A

Table I Summary of the collected test dataset of FRP-RC compressive members

Ref.	No.	l_{type}	P_{cond}	S_{type}	H	A_g	f'_c	ρ_{FRP}	A_{FRP}	n	d_m	E_{frp}	f_{frp}	t_{type}	d_s	Form	s_v	P_{ue}
			e/h		(mm)	(mm²)	(MPa)	(%)	(mm²)		(mm)	(GPa)	(MPa)		(mm)		(mm)	(kN)
De Luca *et al.* (2010)	4	GFRP	0	S	3 000	372100	32.8-43.7	1.0	3721	8	25.4	44.2	608-712	GFRP	12.7	ties	76-305	10750.8-15234.4
Tobbi *et al.* (2012)	5	GFRP	0	S	1 400	122500	32.6	1.9	2327.5	8-12	15.9-19.0	47.6- 48.2	728-751	GFRP	12.7	ties	80-120	3928.5-4067.0
Afifi *et al.* (2014)a	9	GFRP	0	C	1 500	70685.8	42.9	1.1-3.2	777.5-2261.9	4-12	15.9	55.4	934	GFRP	6.4-12.7	spirals	35-145	2804.0-3019.0
Afifi *et al* (2014)b	9	CFRP	0	C	1 500	70685.8	42.9	1.0-2.4	706.8-1696.4	6-14	12.7	140.0	1899	CFRP	6.4-12.7	spirals	35-145	2905.0-3148.0
Tobbi *et al.* (2014)	4	GFRP CFRP	0	S	1 400	122500	35.0	0.8-1.9	980.0-2327.5	8-16	12.7-19.0	46.3-137.0	728-1902	CFRPGFRP	9.5-12.7	ties	67-120	3900.0-5159.0
Mohamed *et al.* (2014)	9	GFRP CFRP	0	C	1 500	70685.8	42.9	1.7-2.2	1201.6-1555.1	8-10	12.7-15.9	55.4-140.0	934-1899	GFRP CFRP	6.4-12.7	spirals hoops	80	2840.0-3019.0
Prachasaree *et al.* (2015)	13	GFRP	0	S-C	500	12271.8-22500.0	20.8	1.4-2.6	319.5-337.5	4	10.0	50.0	735	GFRP	6.0	spirals ties	50	310.0-390.0
Maranan *et al.* (2016)	7	GFRP	0	C	1000-2000	49087.4	38.0	2.4	1192.8	6	15.9	62.6	1184	GFRPCFRP	9.5	hoops-spirals	50-200	1208.0-2063.0
Xiaochun *et al.* (2016)	2	BFRP	0.17-0.67	S	900	14400.0	34.9	1.4	201.6	4	8.0	50.0	1000	BFRP	6.0	ties	100	90.0-270.0
Hales *et al.* (2016)	6	GFRP	0-0.08	C	760-3730	73061.7	90.0	1.6-2.7	1205.5-1979.9	6	16.0	43.0	715	GFRP	10.0	spirals	76	667.0 - 7126.0
Hadi and Youssef (2016)	3	GFRP	0-0.24	S	800	44 100.0	33.2	1.1	507.1	4	12.7	67.9	1641	GFRP	9.5	ties	50	615.0-1285.0
Hadi and Youssef (2016)	6	GFRP	0-0.24	C	800	33006.4	37.0	2.3	759.1	6	12.7	50.0	1200	GFRP	9.5	spirals	30-60	479.0-1309.0
Ali *et al.* (2016)	7	GFRP	0	S	1 650	122500.0	38.4-41.0	1.2-2.5	1580.2-3172.7	8-16	15.9	62.0	1184	GFRP	9.5	ties	75-150	133.0-201.0
Khan *et al.* (2016)	3	GFRP	0-0.24	C	812	33312.3	37.0	3.5	1189.2	6	15.9	56.0	1395	GFRP	9.5	hoops	60	910.0-2812.0
Hadi *et al.* (2017)	6	GFRP	0-0.24	C	800	34636.1	85.0	2.2	761.9	6	12.7	52.0	1190	GFRP	9.5	spirals	30-60	958.0-2721.0
Elchalakani *et al.* (2017)	7	GFRP	0-0.17	S	1200	41600.0	32.7	1.8	761.2	6	12.7	46.3	708	GFRP	6.3	ties	75-250	584.2-1449.0
Hadhood *et al.* (2017)	10	GFRP	0-0.33	C	1500	73061.7	70.2	2.1-3.2	1592.7-2389.1	8-12	15.9	54.9	1289	GFRP	9.5	spirals	80	497.0-4716.0
Hadhood *et al.* (2017)	5	CFRP	0-0.33	C	1500	73061.7	35.0	2.1	1592.7	8	15.9	141.0	1680	CFRP	9.5	spirals	80	529.0-3090.0
Hadhood *et al.* (2017)	5	CFRP	0-0.33	C	1500	73061.7	70.2	2.2	1607.3	8	15.9	141.0	1680	CFRP	9.5	spirals	80	611.0-5120.0
Hadhood *et al.* (2017)	8	GFRP	0-0.33	C	1500	73061.7	35.0-42.9	2.2	1607.3	8	15.9	54.9	1289	GFRP	9.5	hoops	80	366.0-2 935.0
Khorramian *et al.* (2017)	4	GFRP	0-0.3	S	500	22500.0	37.0	1.6	366.7	6	16.0	41.2	783	GFRP	6.0	ties	90	354.1-774.9
Sun *et al.* (2017)	9	GFRP	0.42-0.97	S	1000	45000.0	33.5	1.0	468.0	6	10.0	60.2	689	GFRP	4.0	ties	50	174.0-677.0
Elchalakani *et al.* (2017)	7	GFRP	0-0.17	S	1 200	41600.0	32.7	1.8	761.2	6	12.7	46.3	708	GFRP	6.3	ties	75-250	584.2-1449.0
Hadhood *et al.* (2018)	25	GFRP CFRP	0-0.33	C	1500	73061.7	35.1	2.2-3.3	1607.3-2411.0	8-12	15.9-16.0	54.9-141.0	1289-1680	GFRPCFRP	9.5-12.7	spirals hoops	80	354.0-3090.0
Hadhood *et al.* (2018)	40	GFRP CFRP	0-0.33	C	1500	73061.7	70.2	2.2	1607.3	8-12	15.9	54.9	1289	GFRPCFRP	9.5	spirals hoops	80	354.0-5120.0
Zhang *et al.* (2018)	8	GFRP	0	S	1200	122500.0	50.0	1.3-2.6	1702.7-3234.0	8-12	16.0-18.0	45.0	840	GFRP	8.0-12.0	ties	38-130	4500.0-5670.0
Tabatabaei *et al.* (2018)	5	GFRP	0	C	1 600	70685.8	49.3	1.6	1130.9	6	15.9	51.2	1374	GFRP	9.5	spirals	80	2871.0-3290.0
Tu *et al.* (2019)	8	GFRP	0	S	600	40000.0	32.1	1.1	440.0	4	10.0-14.0	43.7- 46.0	574-735	GFRP	8.0	spirals hoops	30-80	927.7-981.7
Xue *et al.* (2018)	15	GFRP	0-1	S	1800-3 600	90000.0	29.1-55.2	0.9-2.5	810.0-2295.0	4-8	15.9-2.5	39.0- 44.0	654-729	BFRP	8.0	ties	150	300.0-3091.0
Salah-Eldin *et al.* (2019)	4	GFRP	0.2-0.6	S	2000	160000.0	71.2	1.0	1600.0	6	19.0	62.7	1236	GFRP	10.0	ties	150	1367.0-5100.0
Salah-Eldin et *al.* (2019)	4	BFRP	0.2-0.6	S	2000	160000.0	71.2	1.0	1600.0	6	20.0	63.7	1646	BFRP	13.0	ties	150	1309.0-4965.0
Elchalakani *et al.* (2019)	9	GFRP	0-0.29	S	1200	41600.0	26.8	2.2	923.5	6	14.0	59.0	930	GFRP	8.0	ties	75-250	234.0-1357.0
Othman *et al.* (2019)	15	CFRP	0-1	S	1500	22500.0	44.7	1.4-3.6	315.0-810.0	4	10.0-16.0	145.0-151.0	2000	CFRP	6.0	ties	40.0-140.0	113.0-960.0
Dong *et al.* (2019)	12	GFRP	0-0.35	C	1150	36305.0	40.0	0.5-1.1	199.6-399.3	3-6	10.0	59.0	930	GFRP	8.0	spirals	40.0-120.0	296.0-1459.0
El-Gamal *et al.* (2020)	6	GFRP	0	C	1500	41547.6	25.6	1.6-3.8	677.2-1607.8	6-8	12.0-16.0	61.2 - 62.3	1102-1250	GFRP	10.0	spirals	50.0-100.**0**	1055.0-1227.0
Elchalakani *et al.* (2020)	11	GFRP	0-0.35	C	1150	36305.0	34.0	0.5-0.9	199.6-334.0	3-5	10.0	59.0	930	GFRP	8.0	spirals	40.0-120.0	342.0-1286.0
Abdelazim *et al.* (2020)	16	GFRP CFRP	0-0.66	C	1000-2500	73061.7	46.6	2.1	1600.0	8	15.9	61.8	1449	GFRP	9.5	spirals	80.0	371.0-3535.0

Table 1 Continued-

Khorramian *et al.* (2020)	9	GFRP	0.21-0.23	S	1020-3660	62730.0	48.4	2.8-4.8	1800.3-3011.0	6-10	19.0	43.4	963	GFRP	11.0	ties	300.0	844.0-1550.0
Barua *et al.* (2020)	5	GFRP	0-0.34	C	1750	98979.8	37.3-40.7	1.2	1187.7	6	15.9	64.0	1558	GFRP	9.5	spirals	85.0	1 278.0-4224.0
El Messalami *et al.* (2021)	9	BFRP	0-0.44	S	1100	32400.0	28.4	3.8	1257.1	4	20.0	45.9	913	BFRP	10.0	ties	60.0-180.0	315.0-879.0
Bakouregui *et al.* (2021)	24	GFRP BFRP CFRP	0-0.66	C	1500	73061.7	52.0	1.0 - 3.3	759.8-2411.0	6 - 12	12.7-15.9	54.9-144.0	1289-1765	GFRP BFRPC FRP	9.5	spiralshoops	60.0-120.0	440.0-3705.0
Afaq *et al.* (2023)	4	GFRP	0	C	1000	49087.4	31.8	2.4-2.7	1183.0-1364.6	6	15.9	60.0	1237	GFRP	9.5	spirals	50.0	1582.4-5 958.0

Table II Summary of the ranges of data and test results the collected dataset.

Parameters	H (mm)	A_g (mm²)	f'_c (MPa)	ρ_{frp}	A_{frp} (mm²)	n	d_m (mm)	E_{frp} (GPa)	f_{frp} (MPa)	d_s (mm)	S_v (mm)	P_{ue} (kN)
Minimum	500	12272	21	1	200	3	8	39	574	4	30	90
Maximum	3730	372100	90	5	3721	16	25	151	2000	13	305	15234
Average	1456	67539	45	2	1300	7	15	65	1176	9	92	1834
St. deviation	588.65	42889.79	15.82	0.81	687.76	2.29	2.82	30.5	372.49	1.8	49,5	1766.02
Coef. of	0.41	0.64	0.35	0.41	0.53	0.33	0.2	0.47	0.32	0.21	0,54	0.97